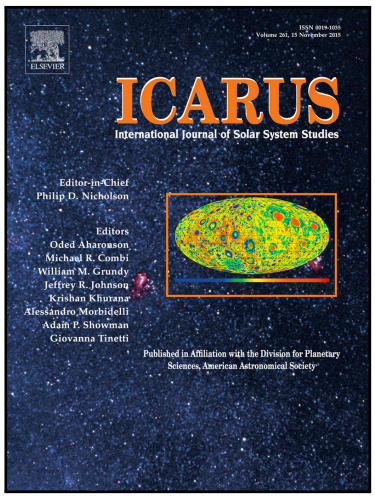

Explosive volcanism on Mercury: analysis of vent and deposit morphology and modes of eruption

Lauren M. Jozwiak , James W. Head , Lionel Wilson

PII: S0019-1035(17)30191-4
DOI: 10.1016/j.icarus.2017.11.011
Reference: YICAR 12695

To appear in: *Icarus*

Received date: 1 March 2017
Revised date: 31 October 2017
Accepted date: 6 November 2017

Please cite this article as: Lauren M. Jozwiak , James W. Head , Lionel Wilson , Explosive volcanism on Mercury: analysis of vent and deposit morphology and modes of eruption, *Icarus* (2017), doi: 10.1016/j.icarus.2017.11.011

Highlights:

- Explosive volcanic morphologies on Mercury are divided into three classes.
- We present analysis of vent dimensions, locations, and stratigraphic ages.
- We find evidence for formation into relatively recent mercurian history.
- We use vent morphology and location to determine formation geometry.
- We find support for eruptions both at and above critical gas volume fractions.

Explosive volcanism on Mercury: analysis of vent and deposit morphology and modes of eruption

Lauren M. Jozwiak[1,2*], James W. Head[1] and Lionel Wilson[1,3]

[1]Department of Earth, Environmental and Planetary Sciences, Brown University, 324 Brook Street Box 1846, Providence, RI, 02912

[2*]Planetary Exploration Group, Johns Hopkins University Applied Physics Laboratory, Laurel, MD, USA.

[3] Lancaster Environment Centre, Lancaster University, Lancaster LA1 4YQ, UK

*Corresponding author: Lauren M. Jozwiak; lauren.jozwiak@jhuapl.edu; 11101 Johns Hopkins Road, Mailstop 200-W230, Laurel MD, 20723-6099.

Resubmitted to *Icarus*

October 31st , 2017

Abstract

The MESSENGER mission revealed, for the first time, conclusive evidence of explosive volcanism on Mercury. Several previous works have cataloged the appearance and location of explosive volcanism on the planet using a variety of identifying characteristics, including vent presence and deposit color as seen in multispectral image mosaics. We present here a comprehensive catalog of vents of likely volcanic origin; our classification scheme emphasizes vent morphology. We have analyzed the morphologies of all vents in our catalog, and recognize three main morphologies: “simple vent”, “pit vent”, and “vent-with-mound”. The majority of vents we identify are located within impact craters. The spatial distribution of vents does not correlate with the locations of volcanic smooth plains deposits, in contrast to the Moon, nor do vents correlate with the locations of large impact basins (except for the Caloris and Tolstoj basins). Using the degradation state of the vent host crater as a proxy for maximum age, we suggest that vent formation has been active through the Mansurian and into the Kuiperian periods, although the majority of vents were likely formed much earlier in mercurian history. The morphologies and locations of vents are used to investigate a set of plausible formation geometries. We find that the most likely and most prevalent formation geometry is that of a dike, stalled at depth, which then explosively vents to the surface. We compare the vent and deposit size of mercurian pyroclastic deposits with localized and regional lunar pyroclastic deposits, and find a range of possible eruption energies and corresponding variations in eruption style. Localized lunar pyroclastic deposits and the majority of mercurian pyroclastic deposits show evidence for eruption that is consistent with the magmatic foam at the top of a dike reaching a critical gas volume fraction. A subset of mercurian vents, including the prominent Copland-Rachmaninoff vent to the northeast of the Rachmaninoff basin, indicates eruption at enhanced gas volume fractions. This subset of vents shows a similar eruptive behavior to the lunar

Orientale dark mantle ring deposit, suggesting that the dikes that formed these vents and deposits on Mercury underwent some form of additional volatile build-up either through crustal volatile incorporation or magma convection within the dike. There also exists a population of mercurian vents that no longer retain a visible associated pyroclastic deposit; we hypothesize that the visible signature of the pyroclastic deposit has been lost through space weathering and regolith mixing processes. Together, these results provide a comprehensive analysis of explosive volcanism on Mercury, and inform continued research on the thermal history of Mercury and magma composition and evolution.

Keywords: Mercury, Surface; Volcanism; Mercury

1. Introduction:

Geologic investigations of the planet Mercury have benefitted immensely in recent years from the wealth of data returned by the MErcury Surface, Space ENvironment, GEochemistry, and Ranging (MESSENGER) mission [Solomon et al., 2007]. Volcanic processes on Mercury have been discussed since the Mariner 10 mission [Strom et al., 1975], which imaged 40% of the planet. Returned images were suggestive of expansive, plains-style volcanism [e.g. Strom et al., 1975] with additional evidence suggested for both explosive volcanism [Robinson and Lucey, 1997] and intrusive magmatic [Schultz, 1977] morphologies. However, a lack of albedo differences between units led to the contrasting interpretation that at least some of the smooth plains deposits were impact-related plains, similar to the Cayley Plains on the Moon [e.g. Wilhelms, 1976]. The debate about the nature of the smooth plains on Mercury remained unresolved and was a central question for the MESSENGER mission [Solomon et al., 2007].

Using MESSENGER's Mercury Dual Imaging System (MDIS) instrument [Hawkins et al., 2007], data from the first flyby of the MESSENGER spacecraft in 2008 revealed extensive evidence for smooth plains-style volcanism [Head et al., 2008; Head et al., 2009a], previously unobserved explosive volcanic deposits, and even a putative example of intrusive magmatic processes [Head et al., 2008]. The explosive volcanic features (vents and deposits) were first observed on the edge of the Caloris basin [Head et al., 2008]; other potential features were subsequently observed on the floors of craters and on plains deposits elsewhere [Kerber et al., 2011]. The explosive volcanic features have been interpreted to be pyroclastic vents on the basis of their irregular and often elongated morphology, lack of associated raised rim, and the mantling morphology displayed by the surrounding deposit, though to be pyroclastic material [Kerber et al., 2009]. Morphometric analysis of these pyroclastic vents observed during the flybys indicated

that the features are significantly larger than observed lunar explosive vents, and the greater areal extent of the associated deposits on Mercury is interpreted to mean that pyroclastic material was emplaced with a higher gas mass fraction than pyroclastic material on the Moon [Kerber et al., 2009]. This result is especially striking given that, prior to the MESSENGER mission, formation models for Mercury [Cameron, 1985; Benz et al., 1988; Boynton et al., 2007; Solomon et al., 2007] suggested that the crust and mantle would be volatile-depleted. Thus, the observation of large numbers of pyroclastic deposits [Kerber et al., 2011] was a surprising result.

In addition to analyses of the spatial sizes of explosively emplaced deposits on Mercury, assessments were also made of the spectral characteristics of the deposits [Goudge et al., 2014] using the Mercury Atmospheric and Surface Composition Spectrometer (MASCS) [McClintock and Lankton, 2007] instrument. Like those of most of the mercurian surface, the deposit spectra are broadly featureless in the visible and near-infrared (VNIR) portion of the spectrum, indicating <2 wt% Fe [Izenberg et al., 2014]. The only identifiable feature in the spectra of Mercury's pyroclastic deposits is a downturn in the UV portion of the spectrum; it was suggested that this feature is related to oxygen–metal charge transfer (OMCT) reactions in the deposits [Goudge et al., 2014]. This investigation also revealed evidence for space weathering of deposits and a gradual reduction in the strength of the UV downturn [Goudge et al., 2014]. The works of Kerber et al. [2011] and Goudge et al. [2014] focused primarily on deposits characterized by a large physical vent and associated color anomaly, and together identified 50 such explosive volcanic landforms in total.

Thomas et al. [2014a] used a global MDIS image mosaic from the first year of orbital data to map all candidate pyroclastic deposits, focusing on the highly characteristic MDIS multispectral mosaic color anomaly found to be associated with pyroclastic deposits on Mercury [e.g., Kerber

et al., 2009]. The study identified 150 vents distributed across the surface of Mercury. Analysis of the correlation of pyroclastic vents with impact crater and basin edges suggested some local correlation (for the Caloris, Beethoven, and Tolstoj basins, and a proposed basin b54 [Fassett et al., 2012]); the authors further note that while the vents are not randomly distributed relative to each other (i.e. vents tend to form clusters), the cluster locations are not spatially correlated with specific geologic landforms [Thomas et al., 2014a]. These previous studies, it should be noted, focused either only on the morphology and eruption mechanism of a subset of the vents [Rothery et al., 2014, Thomas et al., 2015] or on the distribution of vents with no analysis of eruption mechanism [Kerber et al., 2011, Goudge et al., 2014, Thomas et al., 2014a]. Here we present an updated catalog of mercurian pyroclastic vents, with which we analyze vent morphology, discuss implications for eruption conditions, and present constraints on the timing of explosive volcanic activity within Mercury's history.

2. Morphology and Distribution of Mercurian Volcanic Vents

Explosive volcanic deposits on Mercury have been previously identified by various combinations of three distinct criteria (Fig. 1). The first criterion for identification is based upon the morphology of a suspected explosive vent: that is, a depression without a raised rim, morphologically distinct from an impact crater, and often elongate along a single axis (Fig. 1A) [Head et al., 2009a; Kerber et al., 2009, 2011].

The second criterion is the presence of a distinctive color anomaly associated with the deposit [Robinson et al., 2008; Blewett et al., 2009] and visible in processed MDIS color data (Fig. 1B) [Kerber et al., 2009]. As a result of the relative homogeneity of mercurian surface unit albedos, the MDIS team used principle component analysis (PCA) [Murchie et al., 2008; Robinson et al., 2008; Denevi et al., 2009] to develop a standard false-color composite image

that emphasizes different terrains on Mercury. The processing utilizes the following band channels: R: PC 2, G: PC 1, and B: 430/560 nm reflectance [Murchie et al., 2008; Robinson et al., 2008; Blewett et al., 2009]. With this multispectral processing technique, pyroclastic deposits have a bright orange/red color, sometimes called a "red spot" (RS) anomaly, which is useful in identifying previously unrecognized deposits [Kerber et al., 2011, Goudge et al., 2014, Thomas et al., 2014a].

The third possible identifying characteristic is a relatively high-reflectance annulus surrounding the vent structure (Fig. 1C) [Kerber et al., 2009]. This feature is analogous to the "dark halo" features on the Moon, which are low-albedo annuli surrounding pyroclastic vents, interpreted to be composed of pyroclastic material [e.g. Head, 1974; Heiken et al., 1974; Gaddis et al., 1985; Weitz, et al., 1998; Gaddis et al., 2003]. Although the pyroclastic halos on the Moon and Mercury have contrasting reflectance characteristics relative to the surrounding terrain (i.e., dark annulus but light highlands on the Moon, versus light annulus but dark plains on Mercury), the absolute reflectance values for the pyroclastic deposits suggests that they possess similar absolute albedos [Kerber et al., 2009].

We began our analysis by combining the existing catalogs of mercurian pyroclastic vents from Kerber et al. [2009], Goudge et al. [2014], and Thomas et al. [2014a], giving a total of 170 prospective explosive volcanic vents. We used a combination of MDIS WAC (wide angle camera) and NAC (narrow angle camera) monochrome images, as well as MDIS multispectral mosaics comprised of the entire mission data set [Denevi et al., 2013; Domingue et al., 2015] for our observations. This approach represents a significant improvement over the previous catalogs, which were limited to flyby data and data from the first year in orbit. The focus of our investigation was to examine the processes of generation and emplacement of pyroclastic

volcanism on Mercury; as such our catalog consists only of vents of clearly or highly probable explosive volcanic origin. Because of this, and the increased image coverage and resolution, many of the more speculative identifications of possible vents from Thomas et al. [2014a] were reclassified or removed as being of inconclusive explosive volcanic origin or lacking an observable physiographic vent structure. Our final catalog includes 52 more vents than that presented by Goudge et al. [2014], and 65 fewer candidates than Thomas et al. [2014a].

Because of our emphasis on features clearly of an explosive volcanic origin, we considered only those landforms with morphologies consistent with their being a vent, even though the morphological expression of a pyroclastic vent on Mercury varies. Specifically, the presence of a "red spot" (RS) color anomaly was not required for a putative vent to be included in our catalog; similarly, regions with an RS anomaly, but no observable physiographic vent present, were not included in our catalog. Of the three criteria listed above, the high-reflectance annulus is the least consistently observable feature, being highly sensitive to illumination conditions and viewing geometry; as such, a high-reflectance annulus was not required to be present for a candidate depression to be identified as a vent.

2.1 Morphology

From our analysis of these existing pyroclastic vent catalogs, we identified five main morphologic feature types, of which we consider three to be clearly volcanic in nature. We assign the following adjectival descriptors to these five discrete morphologies: "simple vent" (Fig. 2), "pit vent" (Fig. 3), "vent-with-mound" (VwM) (Fig. 4), "shallow pits" (Fig. 5), and "irregular pitted terrain" (Fig. 6). Of these five classes, we regard those landforms with "simple vent", "pit vent", and "vent-with-mound" morphologies to be unambiguously volcanic in origin.

Our final catalog contains 100 pyroclastic vents comprised of these three morphologic sub-types, with the breakdown of each provided in Table 1.

The type of landform that morphologically corresponds to what we term a "simple vent" (Fig. 2) is characterized by an elongate shape in plan view, with a semimajor axis resolvably longer than the semiminor axis, and walls sloping to a relatively narrow floor. We note that the adjective "simple" does not refer to the formation history or setting of the vent, and it is intended solely as a morphological designator. The "simple vent" morphology can occur as a single depression (Fig. 2A), or can occasionally characterize several discrete depressions, interpreted as individual vents, which overlap to form more arcuate features (Fig. 2B). These arcuate features show that it is possible for multiple eruptions to occur within the same region; although it is often difficult to interpret the temporal relationships between these vents. These vents may represent multiple phases of eruption within a single vent, forming a morphology akin to a terrestrial "compound volcano" [Davidson and de Silva, 2000], as suggested by Rothery et al. (2014) for a vent within the Caloris basin (22.3° N, 146.2° E). In contrast, the vents in Fig. 2b suggest multiple discrete eruptions within the same crater, each eruption forming a discrete vent over some unknown interval of time. We determined that 57% of the pyroclastic vent catalog consists of "simple vents".

In contrast, landforms with a "pit vent" morphology (Fig. 3) are characterized by more equant axis lengths and a wider floor profile, and comprise 36% of all landforms in the catalog. The "pit vent" morphology contains features that are circular or elliptical (Fig. 3A), as well as those that have a more complex shape, such as the kidney-shaped pyroclastic vent and deposit to the northeast of the Rachmaninoff basin (Rachmaninoff- Copeland vent) (Weider et al., 2016) (Fig. 3B).

The final morphology included in our catalog of probable volcanic vents corresponds to the type of landform we label as "vent-with-mound"(VwM) (Fig. 4), in which a central mound of material is circumscribed by a prominent vent, and in all cases also has a RS color anomaly. The "VwM"-type feature comprises 7% of the catalog and comes in two submorphologies: circular (Fig. 4A) and irregular (Fig. 4B). The irregular morphologies are situated within the Caloris basin, and the circular morphologies are located outside the Caloris basin (Fig. 4A).

As noted above, two other morphologic classes ("shallow pit" and "irregular pitted terrain") were observed during our characterization, although they were omitted from the final catalog because they could not be unequivocally linked to volcanic processes. The "shallow pit" morphology (Fig. 5) is typified by several (i.e., >3) broadly circular, bowl-shaped pits that are relatively shallow (<200 m depth, or depth indeterminate at the scale of the topographic dataset). These "shallow pits" are usually observed in association with a RS anomaly; where it is observed, however, the RS anomaly is not areally extensive, and a genetic link between the anomaly and the pits is unclear (Fig. 5B). It is possible that landforms displaying the "shallow pit" morphology are highly degraded end-members of another volcanic morphology; however, because its origin is unclear, the "shallow pit" morphology was omitted from our catalog of distinct volcanic vents, although the locations are provided in Table 2.

We have named the final observed morphologic feature type "irregular pitted terrain" (IPT) (Fig. 6) (previously described as "pitted ground" by Thomas et al. [2014a]). This textured terrain has been observed physically on other vent morphologies (Fig. 6B), spatially near other vent morphologies, and as the sole morphologic indication of proposed volcanism in a region (Fig. 6A) [Thomas et al., 2014a]. This morphology can be composed either of multiple pits or a single pit that is irregular in outline and small on the scale of instrument resolution (e.g., pit

diameter of ~1 km compared with MDIS base map resolution of 250 m/pixel [Denevi et al., 2013]). Irregular pitted terrain appears closely associated with RS anomalies, although it is unclear if this association is genetic, or if it is the result of observational bias (i.e., the pits that make up this terrain texture are so small that without a collocated RS anomaly the morphology would not otherwise be noticed). This morphologic feature type is only included in our catalog when the morphology directly overlaps, or has formed on the side of, a larger, more distinct and unequivocal vent (Fig. 6B). One of the major differences between our catalog and that of Thomas et al. [2014a] is that ours omits examples of irregular pitted terrain that occur in isolation or without one of the recognized volcanic morphologies. This terrain texture is morphologically similar to, although distinct from, the "hollows" documented across Mercury (Fig. 6C) [e.g., Blewett et al., 2011; Thomas et al., 2014b], displaying the characteristic red/orange coloration in false color images unlike the blue color associated with hollows. Furthermore, clustered hollows appear to coalesce and form extended flat-floored depressions (Fig. 6C) [Blewett, et al., 2011], whereas IPT depressions do not categorically display flat-floored morphologies. Given the broad morphologic similarity between irregularly pitted terrain and hollows, we agree with the suggestion of Thomas et al. [2014a] that irregular pitted terrain is the result of the sublimation of volatile species within young volcanic deposits (either explosive or effusive in nature). Regardless, this morphologic feature type is not, at this time, an obvious primary volcanic feature, and will not be discussed further in this work (although a listing of all currently identified IPT is provided in Table 3).

2.2 Morphometric Analysis

The majority (93%) of pyroclastic vent morphologies included in our catalog fit the morphologic definition of "simple vent" and "pit vent". We performed a morphometric

examination of these features (e.g., length, width, and depth) to determine if the morphologic differences between these feature types were a function of feature size, and thus perhaps indicative of differences in formation mechanism. From our catalog of 104 vents, we identified and measure 120 simple vent or pit vent segments, as some locations host overlapping, but distinct vents (e.g. simple vent shown in Fig. 2b consists of four simple vent segments in a single location). We used the ArcGIS software package and MDIS complete monochrome basemap (with a resolution of 250 m/pixel [Denevi et al., 2013]) and projected the data in a sinusoidal projection centered on the central longitude of each vent for all measurements. The long axis of the vent was measured to an accuracy of $\pm$500 m (i.e., two pixels, given the resolution of the base map). To measure vent depth, we used topographic data from both the Mercury Laser Altimeter (MLA) (both individual track data and interpolated DEM data) [Zuber et al., 2012], and a digital elevation model (DEM) derived from stereophotoclinometry and utilizing images acquired through the end of 2012 [original reference Gaskell et al., 2008]. Additionally, a global DEM was produced by the USGS; however, the resolution of 2 km/px was insufficient for our morphometric analysis. The German Aerospace Center (DLR) is in the process of producing DEMs based on previously defined Mercury quadrangles [Greely and Batson, 1990]; however this process is not complete, and the first quadrangles were made available after the submission of this manuscript, and consequently could not be included in our analysis. We gave preference to MLA individual track data, where possible, with all other observations supplemented by the interpolated MLA DEM and Gaskell DEM, the latter two datasets providing minimum estimates for vent depth. Vent depth was calculated by taking the average of three profiles across the deepest part of a given vent; this was done to avoid areas of obvious post-formation slumping and infall of material. Data from individual MLA tracks have a vertical accuracy of 1 m and a

horizontal resolution of 20 m [Zuber et al., 2012], whereas all other data (interpolated MLA and stereophotoclinometry-derived DEM) are approximated to the nearest 100 m. Depth data were collected for 106 of the 120 simple vent or pit vent segments.

Morphometric measurements of simple vents and pit vents are provided in the first two rows of Table 4, including average vent length, standard deviation, median length, and mode. The significant overlap in the size range of simple vents and pit vents (Table 4, compare Fig. 7B with Fig. 7C) shows that the morphological differences between these two feature classes are not a function of the length of the feature, that is, simple vents are not characterized by small axes lengths and pit vents by large axes lengths, or vice versa. Instead, the data suggest that there is little morphometric difference in the size of the two features (compare Fig. 7B with Fig. 7C), leading us to conclude that the features are different expressions of a similar formation process. A qualitative assessment of the morphology of what we term pit vents suggests that many of these landforms are more degraded than most simple vents, possessing visually rounded rims, broader floors, and overall muted morphology. For example, the crater Kipling (Fig. 2A) contains both a simple vent (north-south trending vent) and a pit vent (east-west trending vent); the simple vent has a well-defined rim, steep walls, and a narrow floor. In contrast, the pit vent has a more-rounded rim, shallower walls, and a broader floor. The degradation state of the pit vent appears consistent with that of the host crater, unlike the simple vent morphology, which appears fresher than the host crater and nearby pit vent. This raises the prospect that simple vents can degrade into pit vents through time primarily through mass wasting of material from the walls of the vent.

We also examined the average depth of both simple vents and pit vents (Fig. 7D). Goudge et al. [2014] measured the depths of six prominent vents, including both simple vents

and pit vents, although Goudge et al. [2014] describe the landforms simply as "source vents", for which MLA track data were available, and found depths of 1.2–2.4 km, with an average depth of 1.8 km. Rothery et al. [2014] provided depth measurements for two vents inside the Caloris basin, and measured depths of 1.7 km and 1.3 km for the two investigated features. We measured depths for all of the 100 vents in our database and found an average depth of 0.6 km (Table 4), and an overall range of depths from 0.2 km-2.8 km. We suggest that the convergence of depths at 0.5 km (Table 4) can be attributed to the average vertical resolution of ±200 m for the Gaskell dataset. Our data indicate that vents on Mercury are considerably shallower than initially estimated; although because interpolated MLA data and stereophotoinclinometry tend to underestimate depth, these values should be seen as minimum estimates on depth. The depth measurements presented in Goudge et al. [2014] and Rothery et al. [2014] are consistent with our vent depth measurements for four of the six vents; however, our measurements for the Rachmaninoff-Copland vent (35.8°N, 63.8°E) and the unnamed vent located at 58.8°N, 160.6°E (RS-02 in Goudge et al., 2014) indicate these vents are up to 1 km deeper than previously measured. Overall, we attribute the differences in vent depths between the earlier study of Goudge et al. [2014] and our analysis to a numerically larger dataset, featuring the inclusion of vents representing a wide range of degradation states.

2.3 Vent Distribution and Location

The spatial distribution of pyroclastic vents can potentially yield important information about their formation mechanism(s). The global distribution of our identified pyroclastic vent population is shown in Figure 8. Unlike on the Moon, where volcanic features are located primarily in and around large impact basins on the lunar nearside and the farside South Pole–Aitken basin [e.g. Wilhelms, 1987; Head and Wilson, 1992; Schultz, 1976; Jozwiak et al., 2012;

Gaddis et al., 1985; Gaddis et al., 2003; Hurwitz et al., 2013], spatial relationships of pyroclastic deposits on Mercury are not as clearly defined with respect to other prominent landforms.

For example, the Caloris basin (the largest preserved impact structure on the planet) hosts several pyroclastic vents along its inner edge (Fig. 8C), and other basins such as Tolstoj feature some volcanic vents, but the number of such basin-situated vents is low compared with the rest of the global distribution. Figure 8B shows the global distribution of explosive volcanic vents compared with the global distribution of mapped smooth plains units [Denevi et al., 2013]; the smooth plains units are primarily volcanic in nature, although it is likely that impact ejecta-derived smooth plains are also included in the distribution [Denevi et al., 2013]. There is no obvious correlation between the location of explosive volcanic vents and volcanic smooth plains, indeed, there is a striking lack of explosive volcanic vents associated with volcanic smooth plains. Additionally, there is no correlation between the location of explosive volcanic vents and most impact basins. There are only three vents located at the edge of the Borealis Planitia (formerly the northern volcanic plains), despite their being the most extensive and youngest volcanic plains on Mercury [Head et al., 2009a; Ostrach et al., 2015].

The majority of volcanic vents, 82%, are located inside impact craters and basins (81% of simple vents and 83% of pit vents), although only 10% of vents are located in impact basins (D > 250 km) themselves. This similarity in distribution suggests that both types of landform share a similar formation mechanism (as was suggested by our morphometric analysis in Section 2.2), or that if these two classes of landform do indeed have different formation mechanisms, neither is strongly influenced by its regional geologic context. Within most host craters, vents are located in the middle of the crater floor, or adjacent to the central peak region. Of the vents in our catalog, 16% are located on or within ~10 km of lobate scarps, with 10% of the vents in our

catalog being on or at the leading edge of lobate scarps. Lobate scarps are shortening tectonic features interpreted as the surface deformation associated with thrust faults [Strom et al., 1975; Byrne et al., 2014]. Unfortunately, in cases where vents intersect shortening structures such as lobate scarps, the stratigraphic relationship between the two is often unclear. Goudge et al. [2014] assessed cross-cutting relationships between source vents and lobate scarps in four craters, and found clear cross-cutting relationships in two of the craters, but ambiguous cross-cutting relationships in the other two. The use of cross-cutting relationships in this particular setting is particularly difficult as scarps can experience several periods of activation, just as vents may experience several periods of explosive activity. Thus, it becomes almost impossible to identify which structure was formed first, although one can, at times, determine which structure had the final stage of activity, as was done by Goudge et al. [2014]. Fassett et al. [2011] determined that more than 95% of the surface of Mercury is covered by craters greater than 20 km in diameter, and so it might not be surprising that a majority of volcanic vents are located within craters. However, the large percentage (85%) of vents located within craters combined with the paucity of vents located in volcanic smooth plains (Fig. 8B) suggests that craters are a preferred formation environment for mercurian vents. Alternatively, the paucity of vents in smooth volcanic plains might suggest that resurfacing by smooth volcanic plains covered up vents and has inhibited further explosive volcanism in these regions.

3. Timing of Volcanic Activity

The timing of explosive volcanic activity on Mercury has important implications for the thermal evolution of the planet. Dating of large volcanic smooth plains deposits on Mercury such as the Caloris interior volcanic plains [Fassett et al., 2009] and the northern volcanic plains [Ostrach et al., 2015] by crater size–frequency distribution methods suggests an age of ~3.8–3.7

Ga. Whitten and Head [2015a] performed crater density counts, which report the number of craters (N(D)) with diameter ≥D km per 10^6 km^2 [Crater Analysis Techniques Working Group, 1979]. They compared N(20) values on the volcanic plains within Rembrandt basin and on the Caloris interior plains, and found comparable statistics, again suggesting an age of 3.8–3.7 Ga. Crater areal density measures of numerous smooth volcanic plains deposits yield ages not resolvably younger than about 3.5 Ga [Byrne et al., 2016]. This apparent cessation in effusive volcanism coincides closely with the onset of global contraction on Mercury, as given by cross-cutting relations between shortening structures and volcanic plains [e.g., Banks et al., 2015], and it has been hypothesized that the globally compressive tectonic stress regime inhibited the further formation of smooth volcanic plains deposits [Solomon, 1978; Wilson and Head, 2008]. However, it is not yet clear how the explosive volcanic features are related to the evolution of volcanism on Mercury, and whether these features were confined to a specific "volcanic period" on Mercury (akin to the main phase of lunar mare volcanism [e.g. Hiesinger et al., 2011]) or if volcanic vents formed throughout Mercury's history.

Numerous complications arise when attempting to determine relative or absolute crater retention ages for individual pyroclastic deposits. These complications include mitigating the effects of unconsolidated pyroclastic material on impact crater size and preservation [e.g., Luchitta and Schmitt, 1974], as well as the small size of both vents and deposits, which challenge the likelihood of deriving statistically significant crater size–frequency distributions. We employed a proxy method of dating the physiographic vent structures, which relies upon using the inferred degradation state of the crater hosting the vent to place a bound on the oldest age for the feature; this relative stratigraphic method of dating is the same as that employed by Goudge et al. [2014]. Using the principle of superposition, a vent structure must be younger than

the host crater in which it is located; therefore, the relative age of the host crater places an upper bound on the age of the vent. We used the crater degradation state classification scheme of Prockter et al. [2016], in which craters with diameter greater than 40 km are assigned a degradation class from 1 (most degraded) to 5 (least degraded), following the USGS convention (earlier publications used the opposite numbering convention). Craters with diameter less than 40 km were not investigated, as the morphologic markers used to assess degradation state (e.g. ejecta deposits) became too difficult to reliably identify. The crater degradation classes can then be qualitatively related to the five-age chronostratigraphic sequence for Mercury [e.g., Kinczyk et al., 2016], which includes (from oldest to youngest) the Pre-Tolstojan, Tolstojan, Calorian, Mansurian, and Kuiperian periods [Spudis and Guest, 1988]. Because this method relies upon the inferred degradation state of impact craters, we are not able to extend the analysis to vents that are not located in impact craters, or vents located in host craters with diameter less than 40 km. We were able to assign an oldest stratigraphic age limit on 70% of the craters in our catalog (69/104). Figure 9 shows examples of vents located in craters assigned to each of the five crater degradation classes.

The size–frequency distribution plot for host crater age (Fig. 10A) shows that volcanic vents have formed in craters of all degradation states on Mercury, although most occur in craters the degradation states of which correspond to the Tolstojan and Calorian periods. This finding is similar to that by Goudge et al. [2014]. They observed explosive vents in nearly equal numbers of craters of inferred Mansurian, Calorian, and Tolstojan age; our expanded dataset indicates that pyroclastic vents are situated within a larger number of both Calorian- and Tolstojan-aged craters. Plotting the same data divided into simple vent and pit vent morphologies (Fig. 10B) does not reveal a resolvably different trend in vent-host-crater age distribution. However, when

the data are plotted as a percentage of the total crater population for each degradation class (Fig. 10C), it becomes clear that pit vents are predominantly located in host craters of intermediate to older ages (i.e., classes 2–3), and simple vents are predominantly hosted by craters of intermediate to younger ages (i.e., classes 3–5).

The observation of vents within craters with degradation states corresponding to classes 4 and 5 provides evidence for the formation of vent morphologies relatively recently in mercurian history. Indeed, revised age constraints for the Mansurian and Kuiperian systems suggest that the Mansurian system began as recently as ~1.7 ± 0.2 Ga, and the Kuiperian began as recently as ~280 ± 60 Ma [Banks et al., 2017]. The only vent located in a degradation class 5 crater (Tyagaraja, 3.75 °N, 148.8°W) is shown in figure 9E. Although Tyagaraja has been assigned to degradation class 5, it does not possess well-defined crater rays, the characteristic morphology associated with this class [Kinczyk et al., 2016]. Rather, Tyagaraja has been identified as a subset of class 5 craters distinguished by a bright halo, which could be associated morphologically with either degradation class 4 or 5; the authors thus suggest that these craters morphologically straddle the boundary of the Mansurian and Kuiperian periods [Kinczyk, personal communication]. There are ten vents located in craters with a degradation class of 4, associated with the Mansurian period, and images of all of the Mansurian and Kuiperian period host craters with associated vents can be found in the online supplemental material. However, this number should be viewed as a conservative number of Mansurian aged vents because of the previously mentioned limitations of the host-crater stratigraphic dating method. For example, it does not include the 27 km Kuniyoshi crater, suggested by Thomas et al. [2014] to be “earliest Kuiperian” in age [Thomas et al., 2014] based on the well-preserved impact ejecta deposit and crisp terrace morphology. Although we would interpret Kuniyoshi as a Mansurian period crater

because the crater lacks the system-defining bright crater rays [Kinczyk et al., 2016]. In total, the observation of eleven vents in craters associated with both the Mansurian and early Kuiperian period provide continuing evidence for explosive volcanism extending into relatively recent mercurian history.

The morphologies observed in the global pyroclastic vent population suggest a temporal evolution in vent morphology, and a qualitative assessment of vent morphologies supports a variety of degradation states. The apparent transition from simple vents to pit vents with increasing time is consistent with the hypothesis that the former can degrade into the latter with time, suggested in Section II. Despite observations of a qualitative range in vent degradation state, there is no established quantitative measure of vent degradation state, and there is currently no method by which to tie such degradation to the broader Mercurian stratigraphic history.

We interpret the presence of vents in Mansurian and Kuiperian aged craters to suggest that Mercurian explosive volcanism did not cease at ~3.5 Ga but continued thereafter, consistent with the findings of Thomas et al. [2014]. The range of morphologic degradation displayed by the mercurian vents suggests that many are more degraded, and thus likely older, than those located in Mansurian and Kuiperian host craters. One example of this qualitative range in degradation state is observed by means of the presence or absence of a pyroclastic deposit associated with a given vent. Of the 100 vents in our catalog, 33 did not have associated deposits; this finding includes vents with no RS deposit as well as vents where the RS deposit was entirely contained within the vent structure. Plotting the host crater degradation class of those vents without deposits as a percentage of all vents of that age (as inferred from degradation state) (Fig. 11) shows that about 50% of those vents situated within class 2 host craters (and thus corresponding to the Tolstojian period) do not have associated deposits.

The onset of a globally compressive stress state does not appear to have inhibited the formation of explosive volcanic vents [e.g., Thomas et al. 2014a; Byrne et al., 2016]. However, it could be possible that the global compressive stress state thought to have prevailed as the planet began to contract affected other aspects of vent formation, resulting in an outcome such as a reduction in vent size. We examine how vent morphometric dimensions changed with time by considering host-crater degradation state as an upper bound on the timing of vent formation. Figure 12 displays the length of the main vent axis as a function of host crater degradation class. The data do not show a strong correlation between vent length and crater degradation class.

Figure 13 illustrates three possible scenarios for vent formation through Mercurian history: 1) constant formation throughout the planet's history, 2) episodic, interrupted formation corresponding to an older population and a younger population of vents, and 3) dominant formation early in mercurian history, with a declining rate of explosive vent formation following the transition to a globally compressive stress state and thus sporadic formation for the remainder of mercurian history. Of these scenarios we favor the third, the scenario that is most consistent with existing models for the volcanic evolution of one-plate tectonic planets. This scenario for Mercury would reflect the similarly proposed volcanic evolutionary sequence of the Moon (summarized by Head and Wilson, 2017), with a period of effusive and explosive volcanic features emplaced prior to the onset of global compressional stresses [Hiesinger et al., 2011; Hurwitz et al., 2013; Whitten and Head, 2015b], followed by the periodic emplacement of localized non-effusive volcanic structures (e.g. the Compton-Belkovich volcanic complex [Jolliff et al., 2011] and irregular mare patches (IMPs) [Braden et al., 2014]). On Mercury, this would be expressed as a widespread effusive volcanism and explosive volcanism (to an unknown extent)

prior to ~3.6 Ga. After ~3.6 Ga there was waning and cessation of effusive volcanism and either episodic or quasi-continuous (but probably waning) explosive volcanism.

4. Modes of Formation

Having surveyed the morphologies of mercurian pyroclastic vents, their deposits, regional settings, and possible timing of formation, we now investigate the plausible modes of formation. Specifically, we address the likely geometry of intrusive bodies and their subsequent eruption. We propose five candidate modes of formation: 1) a dike propagates to the shallow subsurface, stalls, and forms a sill/laccolith (Fig. 14A); 2) a dike propagates, stalls, forms a sill/laccolith with the dike-tip overshooting the upper level of the sill (Fig. 14B); 3) a dike propagates directly to the surface and erupts (Fig. 14C); 4) a dike propagates, stalls, and vents without concomitant formation of a sill/laccolith (Fig. 14D); and 5) a dike propagates and vents along a critically stressed thrust fault (Fig. 14E). In all cases we envisage dikes as linear features with an overall length greater than their thickness. As is the case with terrestrial dikes, eruptions and vents may form only over a small portion of the dike, where it has come closest to the surface.

Due to the large number of vents situated in craters (85%), we first focus on the possible influences of the host crater environment on the siting of explosive volcanism. A frequency distribution plot of host crater diameter (Fig. 15A, B) shows no strongly preferred host crater diameter. We have not observed vents in craters with $D < 20$ km. However, the simple-to-complex transition in crater diameter occurs on Mercury at ~10 km, and craters in the 10–20 km-diameter range display a range of floor morphologies that have not yet fully transitioned to flat-floored complex crater morphologies [Barnouin et al., 2012]. As a result, the identification of vent morphologies, especially of those lacking RS deposits, within such craters is challenging.

Plotting host crater diameter vs. vent length (Fig. 16A, B) also yields no obvious trend. Together, these findings indicate that the dimensions of a host crater have no observable effect on the size of a pyroclastic vent therein.

Of the vents in our catalog, 62% are located in the middle of a crater floor—either at the physical center of the crater floor (i.e., amongst the central peaks/peak ring mountains) or in the broad central plains of a crater. This distribution is in contrast to the 11.5% of vents that are located along the edge of the crater floor, adjacent to the inner wall. This 11.5% total includes vents in five craters, with five vents located in a single crater, Sher Gil crater (45.1° S, 225.5° W) (Fig. 17). We observed no evidence of crater floor fracturing in the manner similar to that occurring in floor-fractured craters on the Moon [e.g. Schultz, 1976; Jozwiak et al., 2012].

There are, however, sets of fractures present in the centers of certain basins that have been filled by lavas (e.g. Rachmaninoff: Prockter et al., 2010), with these structures interpreted to have resulted from the cooling and contraction of those volcanic plains deposits [Blair et al., 2012; Freed et al., 2012]. Similarly, many ghost craters (craters that have been buried by volcanic flows and are identified by the ring-shaped deformational structures marking the rim location [e.g. Head et al., 2008; Watters et al., 2009]) in the northern volcanic plains exhibit fractured surfaces, features again likely to be related to the solidification of ponded lavas [Head et al. 2011; Freed et al., 2012; Watters et al., 2012]. The center of the Caloris basin also hosts an extensive, radial fracture network, Pantheon Fossae, which may be an extensional system formed in response to upwelling beneath the basin [Head et al., 2009b], possibly analogous to coronae on Venus [Squyres et al. 1992], although Klimczak et al. [2010] have suggested that the graben associated with Pantheon Fossae are not consistent with an intrusive magmatic formation. With the exception of those within Tolstoj and Rachmaninoff basins, and possibly some within Caloris

[Rothery et al., 2014], no vents are associated with these fracture structures. It may be that once-visible fractures were covered by subsequent smooth plains emplacement (either volcanic or impact-derived), but we find it unlikely that resurfacing would cover signs of floor deformation (like fracturing and uplift) yet preserve pyroclastic vents and deposits.

In our first proposed formation geometry, a dike propagates from depth, stalls in the shallow subsurface, and forms a sill/laccolith (Fig. 14A); this is the formation mechanism of floor-fractured craters on the Moon [Schultz, 1976]. In the lunar case, this intrusion geometry produces an uplifted/domed floor, concentric and/or radial floor fractures, and eruptions can lead to volcanic landforms such as mare deposits and pyroclastic deposits [Jozwiak et al., 2012; 2015a]. The bending stresses associated with the edges of the sill/laccolith morphology result in the localization of volcanic features over these edges — that is, close to and parallel with the crater wall [Johnson and Pollard, 1973]. As discussed above, there is no evidence on Mercury for either uplifted/domed floors or wide-scale floor fracturing in craters that host pyroclastic vents. Furthermore, the majority of pyroclastic vents located in mercurian craters are located at or near the center of the crater floor, which is an unfavorable location for the propagation of a subsidiary dike from a sill. It is possible to explain the lack of surface uplift and fracturing by invoking either deeply seated sills [Thomas et al., 2015b] or a lopolith morphology (the inverse of a laccolith morphology, wherein the strata underlying the intrusion are deformed downward, as opposed to the upward deformation of strata associated with laccoliths). However, neither explanation accounts for most pyroclastic vents occurring in the center of craters. Although a shallow sill geometry is plausible for the vents in crater Sher Gil (Fig. 17), overall we find it improbable as a mechanism to explain the majority of explosive volcanic vents on Mercury.

The second formation model, the "sill with dike overshoot" geometry (Fig. 14B), is similar to the first scenario (compare Fig. 14B to Fig. 14A) with the addition of the dike tip overshooting the level of sill formation. As before, the formation of a sill or laccolith in the shallow subsurface results in floor uplift and associated tectonic deformation, which is not observed in association with the mercurian pyroclastic vent craters. However, the overshoot of the dike tip would allow for eruptions and venting at any possible location within the crater, including in the center of the crater, although one would predict only one dominant eruption site in each crater. Thus, if paired with a deep-seated sill, this model geometry could plausibly recreate instances where there is a single volcanic vent within a host crater without associated doming (Fig. 18). Multiple, discretely located vents within a single crater are difficult to account for with this geometry because of the reliance on eruption of the dike tip to form the main vent, such that any subsequent vents would be confined to wall-adjacent positions from subsidiary diking from the edge of the sill.

The next two model geometries are closely related and describe a dike propagating to the surface (Fig. 14C) or stalling in the shallow subsurface (Fig. 14D) before venting. Several factors govern whether a dike will propagate to the surface or stall, including magma composition and volatile content, local lithospheric stress conditions, crustal thickness, and mechanical strength of the surrounding host rock [e.g. Rubin and Pollard, 1987; Rubin, 1995; Wilson and Head, 2017]. Magma composition and volatile content are particularly important, as these variables affect magma density, and volatile degassing also influences eruption style. As the dike approaches the surface, decreasing confining pressure leads to the degassing of any volatile species within the melt [e.g., Sparks 1978]. If the volume fraction of gas (in the form of bubbles) exceeds a critical gas volume fraction (60–90% [Vergniolle and Jaupart, 1990]) an

explosive eruption and dispersal of pyroclasts will take place. Head and Wilson [2017] illustrated how isolated pits with a variety of geometries (circular, elongated, or irregular) can be produced — by collapse along the top of a dike in response to volatile release, explosive dispersal of material in an eruption, or a combination of both processes, in which collapse follows explosive eruption of volatiles in the top of the dike. The final morphology of the vent is then a function of the width of the dike and the depth at which it stalled [Head and Wilson, 2016]. In cases where a portion of the dike reaches the surface, we predict a clear, simple vent morphology to result, with the long axis of the vent aligned with the portion of the dike that intersected the surface. In cases where the dike stalls in the subsurface before venting, we predict a wider range of vent morphologies including a less prominent elongation for both simple vents and pit vents.

The vent geometries resulting from surface-breaking or shallow dikes (Fig. 14C, D) are capable of forming in a multitude of orientations relative to the host crater, because the dike orientation will not be strongly controlled by a local stress field. Shallow or surface-breaking dikes also allow for the formation of multiple vents in the same crater, each from a discrete feeder dike. Furthermore, unlike the sill models (Fig. 14A, B), the dike models would not be expected to cause widespread uplift of the associated host crater floor, satisfying a key observation of mercurian pyroclastic vent host craters. A primary expected morphologic difference between the two dike-only models is the formation of associated graben or pit crater chains, which may result from extension over a very shallowly seated dike [Head and Wilson, 1993; Petrycki and Wilson 1999a, b; Wilson et al., 2011; Hardy, 2015; Head and Wilson, 2016]. The dike may remain stalled entirely within the crust (Fig. 14D), or some portion of the dike may intersect the surface and vent (Fig. 14C). Head and Wilson [2016] outlined several mechanisms by which shallowly stalled dikes may vent to form graben and pit crater chains. Under lunar

conditions, for example, dikes stalling within a few hundred meters of the surface are likely to produce graben [Head and Wilson, 2016]. We do not observe either graben or pit crater chains associated with the mercurian pyroclastic vents, leading us to favor a formation geometry of a dike stalled at greater than a few hundred meters below the surface. Consequently, the stalled dike venting model (Fig. 14D) can plausibly explain the morphologies of the majority of mercurian pyroclastic vents.

The final model geometry we consider is propagation of a dike along a thrust fault (Fig. 14E), either along the entire vertical extent of the fault, or in the immediate shallow crustal environment. It has long been suggested [Strom et al., 1975; Melosh and McKinnon, 1988], and new observations from MESSENGER confirm [Byrne et al., 2014], that the dominant global tectonic regime for the majority of Mercury's history has been compressive. Net horizontally compressive environments inhibit magma ascent [e.g. Solomon 1977, 1978; Head and Wilson, 1992], and because of this previous workers [Head and Wilson, 2008] suggested that volcanic activity on Mercury would cease following the transition to global compression. In terms of major effusive activity, this has been shown to be the case for Mercury [Byrne et al., 2016]. However, the discovery of young effusive volcanism in the Rachmaninoff basin [Prockter et al., 2010] and the observations of explosive volcanic vents in stratigraphically young craters [Kerber et al., 2011; Goudge et al., 2014; Thomas et al., 2014a; this work] gives clear evidence for continued, albeit small-scale, volcanic activity into recent (~ 1 Ga) mercurian history.

To accommodate magma transport in a compressive tectonic regime, previous workers suggested that magma would be most efficiently transported along pre-existing faults to reach the surface [e.g., Klimczak et al., 2013; Thomas et al., 2015b]. Klimczak et al. [2013] observed that, of the then-recognized volcanic vents and deposits, 37% were located within 30 km of a

thrust fault, which the authors interpreted as support for magma transport along critically stressed faults (i.e., faults whose stress state put them on the verge of slipping). Modeling work [e.g., Ziv et al., 2000] has been done on the problem of magma transportation along preexisting faults. Ziv et al. [2000] found that the process of magma transport along a preexisting fault is difficult to achieve, and is dependent on the ratio of effective ambient dike-normal stress (either compressional or tensile) and the host rock tensile strength, the ratio of shear stress resolved on the fault to the magma pressure, and the orientation of the fault itself relative to the least compressive stress. In the cases of mid-to-lower crustal depths, the effective ambient stresses on the propagating dike become much larger than the rock tensile strength, making it extremely difficult for the emerging dike to follow an existing fault [Ziv et al., 2000]. These workers suggested that dike propagation along a preexisting fault only becomes viable in environments where the ambient effective compressive stress is low and shear stress along the dike walls is small, such as the upper few kilometers of a planetary crust. These results suggest that the transport of magma along faults from the low-to-mid crustal depths is unlikely; this conclusion is amplified for earlier periods of Mercury's history when a shallower brittle-ductile transition would have inhibited fault formation altogether in the lower crustal region. However, transportation along preexisting faults in the shallow subsurface might be tenable, especially if those faults are critically stressed (such that the resolved shear stress on the fault is low), and if the fault is oriented relatively close to perpendicular to the least compressive stress. The last point is particularly important for the mercurian setting, as many of the large thrust faults are suggested to have low dip angles [e.g. Watters et al., 2002], thereby orienting them perpendicular to a vertical least compressive stress, and making them more favorable to magma transport.

In our catalog, 10% of the vents were located on top of, or at the leading edge, of a lobate scarp (interpreted as the surface deformation associated with a thrust fault) (e.g. Fig. 19, 20)—and these vents are candidates for near-surface magma transport along preexisting fractures (Fig. 14E). For these 10% of vents, stratigraphic relationships between the vents and the faults are difficult to discern. Goudge et al. [2014] observed, for both the vent in Enheduanna crater (referred to as NE Derzhavin in Goudge et al., 2014) and the vent in Glinka crater, that the vents were cross-cut by the scarps, indicating that the vents pre-dated the last phase of scarp activity; however, for two additional vents the cross-cutting relationships were ambiguous. Thus, although those 10% of vents located along thrust fault-related landforms are candidates for near-surface magma transport along faults, it is unlikely that all of the vents formed in this manner. For the remaining 90% of vents in our catalog that are not obviously spatially associated with scarps, formation by magma transport along preexisting fractures is unlikely.

The dike-venting model (Fig. 14D) can plausibly produce both simple vent and pit vent morphologies by variations in parameters such as depth of dike stalling and dike width. The depth at which a dike stalls is correlated with the width of overlying negative-relief features such as graben, such that deeper stalled dikes yield wider and shallower graben [Head and Wilson, 2016]. The primary morphologic difference between simple vents and pit vents is the difference in aspect ratio, with simple vents having more elongate forms, and pit vents having axes of more equant dimensions. While our morphometric analyses from Section 2 suggest that simple vents may degrade through mass-wasting processes into pit vent morphologies, this process is not plausible for all pit vents. Pit vents possessing particularly large, broad floors (in excess of several kilometers) (e.g. the Rachmaninoff-Copland vent, Fig. 3B), are not likely to have ever resembled simple vent morphologies. Applying the dimension criteria to the dike stalling model

suggests that simple vents form from venting of dikes that stalled in the relatively shallow subsurface (Fig. 21A), and broad-floored pit vents form from dikes that stalled at relatively greater depths (Fig. 21B).

The circular vent-with-mound (VwM) (Fig. 4A) morphology remains enigmatic, and is not well explained by any of the proposed formation geometries examined above (Fig. 14). Thomas et al. [2015a] hypothesized that this morphology is the result of magma transport and eruption along faults circling the central peak of craters. In this scenario the eponymous "mound" is, in fact, the residual central peak of the crater, and the large volume of the mound arises from the volume of the central peaks combined with the excavation of material beneath the crater floor (i.e. the mound is formed by the removal of material from the crater floor, not the additional of material to form a mound). The model of Thomas et al. [2015a] is non-committal about whether the entire vent forms in a single eruption, or proceeds in a piecemeal fashion. Our morphologic analysis has observed several examples of vent formation adjacent to and partially encircling central peaks wherein the peaks retain both their morphology and their original elevation (Fig. 20). In these examples, several vents can also be identified that have overlapped to form the overall structure. This suggests that the VwM structure may be viewed as one end member of a continuum for eruptions in the central peak region of a crater. One extreme of the continuum contains a single vent (e.g. Fig. 18), and the other extreme contains several overlapping vents eventually surrounding the central peak of a crater (e.g. Fig. 4a). We would also suggest that the hypothesized sill formation is unnecessary, as there is little morphologic evidence for the floor deformation that would be associated with sill emplacement. Additionally there is no morphologic evidence for subsidence following the eruption of a large volume of gas-rich magma. Thus, we support broadly the model of Thomas et al. [2015a], but without magma

storage, as a plausible mechanism for forming the VwM features, and as an extreme end-member of the dike-venting formation model for mercurian pyroclastic vents.

For the irregular (non-circular) vent-with-mound (VwM) morphologies observed in the Caloris basin (Fig. 4B), we suggest that the initial vent is formed by eruption from a dike that reaches the surface, followed by a relatively smaller effusive phase that partially fills the vent, but does not breach the structure. This interpretation is supported by the initial simple vent morphology of the inner depression, such that the elevations of these mounds do not exceed the height of the depression in which they are located, and the observation that the infilling mound material does not extend to the edges of the host vent but rather collects in the center of the vent.

Based on our morphologic analyses, we support a dike-venting model as the formation geometry for the majority of mercurian pyroclastic vents. We now turn to an analysis of the eruption process, and how understanding the eruption dynamics of these systems might help distinguish between dikes propagating to the surface before venting and those that stall in the shallow subsurface and vent some time later.

5. Eruption Process

The three possible sources for eruption-driving volatiles that we will examine are: 1) degassing of volatile species within the magma, sourced from the melting of the mercurian mantle; 2) formation of volatile species by chemical reactions within the melt (e.g., CO on the Moon [Sato, 1979; Fogel and Rutherford, 1995]) or between the melt and incorporated crustal material [Zolotov, 2011]; and 3) volatile build-up as a result of magma cycling and convection within a stalled dike [Head et al., 2002].

Kerber et al. [2009] measured the deposit radius for the large pyroclastic deposit located to the northeast of the Rachmaninoff basin (referred to also as either the Rachmaninoff-Copeland vent or the NE Rachmaninoff vent by the MESSENGER team) (Fig. 3B). Using the maximum distance of pyroclastic material from the vent, the ballistic trajectory equation, and accounting for differences in gravity between the Moon and Mercury, the authors determined that emplacing the Rachmaninoff-Copeland vent deposit would require the equivalent ~5500 parts per million (ppm) CO compared with 2400 ppm CO on the Moon [Kerber et al., 2009]. The data thus suggest that, at the time of eruption, mercurian eruptions had a higher volatile content than lunar eruptions. We expanded this analysis to our catalog of pyroclastic vents, assessing deposit radius as a function of vent length. The deposit radius was measured using MDIS PCA color mosaic images. The plotted deposit radius is the average of 6 radial profiles measured at 60 degree intervals of azimuth from the center of the vent to the visually determined edge of the deposit.

Figure 22A shows the deposit radius as a function of vent length for pyroclastic deposits on both the Moon (red squares) and Mercury (blue diamonds). The lunar data were collected in the same manner as the mercurian data, and represent localized pyroclastic deposits on the floors of the craters Alphonsus, Oppenheimer, Schrödinger, and Gauss [Gaddis et al., 2003]. We restricted our lunar analysis to these deposits as they have a clearly defined albedo anomaly and a distinct central vent.

Analysis of the deposits in Alphonsus crater suggest that the eruptions had a gas volume fraction of 72.8% [Jozwiak et al., 2015b], consistent with experimental ranges for critical gas volume fractions necessary to initiate explosive eruptions [Jaupart and Vergniolle, 1989]. This finding in turn suggests that the trend defined by the lunar data represents eruptions driven by the collapse of a critically gas-rich magmatic foam. The data for Mercury show significantly more

scatter than the lunar data; the lunar data have an R^2 value of 0.97 from a best fit trendline, while mercurian data have an R^2 value of 0.13. Several mercurian deposits plot along the *x*-axis; these are vents for which there is no obviously associated deposit (discussed previously in Section 3). Such examples represent a notional vent end member, for which an associated deposit likely formed but was then weathered with time due to regolith mixing and is no longer detectable. In addition to space weathering processes, the increased regolith thickness on Mercury compared with that on the Moon, together with related mixing processes [Kreslavsky and Head, 2015] also act to decrease the observed deposit radius.

The localized lunar pyroclastic deposits plotted in Fig. 22A are the smaller of the two recognized types of pyroclastic deposit on the Moon, the other type being regional pyroclastic deposits [e.g., Gaddis et al., 1985], which have areas >1000 km^2. As described above, the localized pyroclastic deposits are assumed to be formed in short-lived vulcanian-style eruptions (gas-dominated eruptions driven by significant volatile enrichment and eruption through country rock) [e.g., Head and Wilson, 1979; Wilson and Head, 1981; Hawke et al., 1989; Weitz et al., 1998]. Calculations of gas volume fraction for these lunar eruptions [Jozwiak et al., 2015b] indicate that such activity occurs after a critical gas volume fraction is reached. In contrast, regional pyroclastic deposits are hypothesized to form in the lunar equivalent of more energetic Hawaiian-style fire-fountain eruptions [Wilson and Head, 1981; Weitz et al., 1998] (e.g., Aristarchus plateau [Head and Wilson, 2016]) from dikes emplaced into the near-surface crust [Head et al., 2002; Wilson et al., 2011; Wilson et al., 2014]. In the latter case, wide dikes stall in the subsurface and convection within the dike allows magma in the lower part of the dike to degas, increasing the gas bubble concentration in the upper part of the dike [Head et al., 2002; Wilson et al., 2011; Wilson et al., 2014]; when the eruption finally occurs, the greatly increased

gas concentration ejects pyroclasts to distances beyond 100 km from the vent [Wilson et al., 2014]. The Orientale Dark Mantle Ring Deposit (DMRD) (30° S, 97.7° W) is the type example of this eruption mechanism [Head et al., 2002]. Using the basis by which localized and regional lunar pyroclastic deposits are defined, we proposed two possible volatile evolution scenarios for Mercury: 1) gas exsolved locally from magma builds up until the critical gas volume fraction is reached, triggering foam collapse and eruption; and 2) gas continues to build up and thicken the magmatic foam region at the top of a trapped, pressurized dike, beyond the critical volume fraction, eventually triggering a more energetic eruption.

To compare more directly the processes on the Moon and Mercury, we use the ballistic trajectory equation (Eq. 1) to calculate the pyroclast ejection velocity, *v*, from the radius, *R*, of a given deposit, using

$$v = \left(\frac{Rg}{\sin 2\theta}\right)^{1/2} \quad \text{Eq. 1}$$

The gravitational acceleration, *g*, is 3.7 m/s^2 for Mercury and 1.62 m/s^2 for the Moon. The angle of ejection, θ, is assumed to be 45°, representing the maximum dispersal distance. By plotting the ejection velocity for the pyroclastic deposits we effectively remove the effects of gravity scaling, and can more closely compare the trends for the lunar and mercurian data.

Figure 22B shows the pyroclastic ejection velocity as a function of vent size for the lunar dark halo craters (red squares), Orientale DMRD (green triangle), and mercurian vents (blue diamonds). As before, we have plotted a trend line through the lunar dark halo craters, this trend representing eruptions at the critical gas volume fraction (scenario 1, wherein locally exsolved gas builds up until the critical gas volume fraction is reached). A considerable number of mercurian vents cluster around this trend, suggesting that the dikes feeding these eruptions

vented after reaching the critical gas volume fraction. Falling below the trend line (dashed black oval) is a cluster of data with lower than predicted ejection velocity. We interpret these data to result from deposit erasure and mixing processes. It is unknown where these vents would have originally plotted, but we see no reason to attribute the perceived lower velocity to a separate, unusually volatile poor source magma, although our data cannot rule out that possibility. An example of the deposit erasure and mixing hypothesis interpretation can be seen in the crater Picasso (Fig. 23). The northernmost vent is associated with the most-prominent red spot deposit (Fig. 23A, black arrow), and also retains the freshest edge and interior morphology (Fig. 23C, black arrow). In contrast, the southernmost vent has little color evidence for a red spot deposit, and shows signs of morphologic degradation with subdued vent edges and wall material (Fig. 23C, white arrow).

There is also a population of vents plotting above the trend line (solid black oval), indicative of a higher-than-expected volatile content, consistent with scenario 2 (eruption following increases in gas concentration surpassing the normal critical gas volume fraction). As we would expect, the Orientale DRMD plots in the middle of this group. We suggest that the mercurian vents that plot in this field have also undergone additional gas concentration processes within a stalled dike, and that this accounts for the large eruption velocity and correspondingly large deposit radius. The NE Rachmaninoff vent plots within this population, which is consistent with unusually high gas content calculated by Kerber et al. [2009]. A scenario under which gasses become concentrated within the upper portion of a stalled dike, thus driving spatially extensive eruptions, does not appear to be confined to large mercurian vents, as numerous mercurian vents with diameters of about 10 km also plot within this field.

The volatile species driving the eruptions are still not well characterized; however, recent results from the MESSENGER x-ray spectrometer (XRS) and neutron spectrometer (NS) suggest C and S as candidate elements. XRS observations targeted on the expansive pyroclastic deposit associated with the Rachmaninoff-Copeland vent show an anomalously low S/Si ratio [Weider et al., 2016]; similarly, NS measurements targeted on pyroclastic deposit indicate a 1–2 wt% depletion in C, relative to average mercurian values [Peplowski et al., 2015]. Weider et al. [2016] suggested that these depletions are attributable to oxidation of C and S in mercurian magmas; these volatile species are then explosively vented and lost, resulting in the observed depletions. Weider et al. [2016] estimated that 2.5 wt% S and 4.7 wt% CO were lost in the Rachmaninoff-Copeland vent forming eruption, and these workers suggested that incorporation of country rock could serve as a source for the oxides necessary for volatile oxidation [e.g., Zolotov et al., 2011]. Our data are consistent with this interpretation, and the hypothesis of crustal assimilation as a source for additional volatiles [Zolotov et al., 2011] is a viable mechanism for the volatile build-up processes necessitated by scenario 2. However, we strongly caution that our data also suggest that these values are not likely to be representative of, and are overestimations of, the concentration of volatiles in the source magma for the majority of mercurian pyroclastic eruptions. The amount of additional volatile build-up is likely to be unique to each deposit (for example, the regional lunar pyroclastic deposits display a wide range of eventual gas volume fractions [Head et al., 2002; Wilson et al., 2011; Wilson et al., 2014]), and thus the results from the Rachmaninoff-Copeland vent deposit are representative only of that singular eruption. Future work should seek to constrain the volatile percentage that can be incorporated from crustal materials for explosive volcanic activity on Mercury in general.

6. Conclusions

The discovery and confirmation of explosive volcanism on Mercury is one of the most important and unexpected results of the MESSENGER mission. Prior to that mission, models for the formation of Mercury [e.g., Cameron, 1985; Benz et al., 1988; Boynton et al., 2007; Solomon et al., 2007] predicted that the crust and mantle would be relatively poor in volatiles, making explosive volcanism extremely unlikely. In addition, the thin mantle and pervasive compressive stress regime [Strom et al., 1975; Melosh and McKinnon, 1988] would yield a volcanic history dominated by large effusive plains deposits that ceased formation upon the onset of global contraction [e.g., Solomon, 1978; Head and Wilson, 2008]. Thus the discovery [Head et al., 2008] and subsequent ability to quantify [Kerber et al., 2009, 2011; Goudge et al., 2014; Thomas et al., 2014a] numerous examples of explosive volcanism was not expected. Our research has built on the identifications and distributions [Kerber et al., 2009, 2011; Goudge et al., 2014; Thomas et al., 2014a] of explosive volcanic vents to analyze morphology, morphometry, and distribution of the explosive volcanic vents and associated deposits to construct a robust catalog of mercurian pyroclastic landforms. We have also considered hypotheses relating to the formation of the geometries and eruption processes of these vents. We can summarize our findings as follows:

1. Explosive volcanic morphologies can be divided into three major morphologic classes that we term simple vent, pit vent, and vent-with-mound.

2. With the exception of vents located in the Caloris Planitia region, we observe no spatial correlation between mercurian pyroclastic vents and mercurian smooth plains deposits, unlike the association between pyroclastic deposits and maria on the Moon [Gaddis et al., 2003].

3. The majority of volcanic vents are located within craters. We hypothesize that the resetting of regional compressive stresses around the crater helped to allow (and govern) dike propagation, and facilitated continued explosive volcanic activity under a stress regime otherwise unfavorable to magma ascent. The continued formation of explosive volcanic deposits after the transition to global contraction is evidenced by observations of vents and deposits in craters with degradation states that correspond to the Mansurian and Kuiperian periods.

4. The morphologies and locations of a majority of pyroclastic vents on Mercury are consistent with the venting of relatively deeply (i.e., more than a few hundred meters) stalled dikes.

5. An analysis of vent dimensions and pyroclastic deposit dimensions for both the Moon and Mercury suggests that vents on both bodies formed from the explosive venting of stalled dikes. Both bodies have evidence for vulcanian-style eruptions after gas volume fractions exceeded critical values, and both also show evidence for some vents having formed from the continued build-up of volatiles within a dike above the critical fractions observed in the smaller vulcanian-style eruptions, leading to greater dispersal of pyroclasts than in the vulcanian-style scenario. Some mercurian vents also appear to have experienced partial or complete erasure of their associated pyroclastic deposits with time, likely because of space weathering and regolith mixing.

A comparative analysis has revealed interesting parallels between lunar and mercurian explosive volcanism, but differences between the two bodies also raise additional questions. Why do stalled mercurian dikes not form sills like those observed in floor-fractured craters on the Moon [Jozwiak et al., 2012; 2015, Thomas et al., 2015b]? What is the source for the volatiles driving eruptions, especially in the cases of the mercurian vents where it appears no

additional volatile build-up processes have taken place? What has allowed the continuation of volcanic activity up to the relatively recent history of Mercury? This research has provided important new information about the history and character of volcanism on Mercury, and will help inform future efforts to explore the structure, composition, and thermal evolution of the planet, such as that by the upcoming BepiColombo mission to Mercury [Benkhoff et al., 2010].

Acknowledgments: The MESSENGER mission is supported by the NASA Discovery Program under contract NAS5-97271 to The Johns Hopkins University Applied Physics Laboratory and NASW-00002 to the Carnegie Institution of Washington. Also providing support for this work were NASA grants NNX09AQ43G, NNX11AQ47G, NNX12AQ73G, and the MESSENGER Participating Scientist Program through grant NNX08AN29G. We gratefully acknowledge the support of NASA Harriet G. Jenkins Fellowship (Grant NNX13AR86H) to L.M. Jozwiak. Additionally, we thank Jay Dickson for his invaluable assistance in data processing.

References:

Banks, M. E., et al., 2015. Duration of activity on lobate-scarp thrust faults on Mercury. JGR Planets, 120, 1751–1762.

Banks, M. E., et al., 2017. Revised constrains on absolute age limits for Mercury's Kuiperian and Mansurian stratigraphic systems. JGR Planets 122, 1010-1020.

Barnouin, O. S., et al., 2012. The morphology of craters on Mercury: results from MESSENGER flybys. Icarus 219, 414-427.

Benkhoff, J., et al., 2010. BepiColombo—comprehensive exploration of Mercury: mission overview and science goals. Planet. Space Sci. 58, 2-20.

Benz, W., Slattery, W. L., Cameron, A. G. W., 1988. Collisional stripping of Mercury's mantle. Icarus 74, 516-528.

Blair, D. M. et al., 2012. The origin of graben and ridges in Rachmaninoff, Raditladi, and Mozart basins, Mercury. JGR Planets, 118, 47–58.

Blewett, D. T., et al., 2009. Multispectral images of Mercury from the first MESSENGER flyby: analysis of global and regional color trends. Earth and Planet. Sci. Lett. 285, 272-282.

Blewett, D. T., et al., 2011. Hollows on Mercury: MESSENGER evidence for geologically recent volatile-related activity. Science 333, 1856-1859.

Boynton, W. V., et al., 2007. MESSENGER and the chemistry of Mercury's surface. Space Scpi. Rev. 131, 85-104.

Braden, S. E., et al., 2014. Evidence for basaltic volcanism on the Moon within the past 100 million years. Nat. Geosci. 7, 787-791.

Byrne, P. K., Klimczak, C., Sengör, A. M. C., Solomon, S. C., Watters, T. R., Hauch, S. A. II, 2014. Mercury's global contraction much greater than earlier estimates. Nature Geosci. 7, 301-307.

Byrne, P. K., et al., 2016. Widespread effusive volcanism on Mercury likely ended by about 3.5 Ga. GRL, 43, 7408–7416.

Cameron, A. G. W., 1985. The partial volatilization of Mercury, Icarus 64, 285-294.

Crater Analysis Techniques Working Group, 1979. Standard techniques for the presentation and analysis of crater size-frequency data. Icarus 37, 467-474.

Denevi, B. W., et al., 2013. The distribution and origin of smooth plains on Mercury. J. Geophys. Res. Planets 118, 891-907.

Domingue, D. L., Murchie, S. L., Denevi, B. W., Ernst, C. M., Chabot, N. L., 2015. Mercury's global color mosaic: an update from MESSENGER's orbital observations. Icarus 257, 477-488.

Fassett, C. I., et al., 2009. Caloris impact basin: exterior geomorphology, stratigraphy, morphometry, radial sculpture, and smooth plains deposits. Earth Planet. Sci. Lett. 285, 297-308.

Fassett, C. I., Kadish, S. J., Head, J. W., Solomon, S.C., Strom, R. G., 2011. The global population of large craters on Mercury and comparison with the Moon. Geophys. Res. Lett. 38, L10202.

Fassett, C. I., et al., 2012. Large impact basins on Mercury: global distribution, characteristics, and modification history from MESSENGER orbital data. J. of Geophys. Res. 117, E00L08.

Fogel, R.A., Rutherford, M.J., 1995. Magmatic volatiles in primitive lunar glasses: I. FTIR and EPMA analyses of Apollo 15 green and yellow glasses and revision of the volatile-assisted fire-fountain theory. Geochim. et Cosmochim. Acta 59. 201-125.

Freed, A. M. et al., 2012. On the origin of graben and ridges within and near volcanically buried craters and basins in Mercury's northern plains. JGR Planets, 117, E00L06.

Gaddis, L. R., Pieters, C. M., Hawke, B. R., 1985. Remote sensing of lunar pyroclastic mantling deposits. Icarus 61, 461-489.

Gaddis, L.R., Staid, M.I., Tyburczy, J.A., Hawke, B.R., Petro, N.E., 2003. Compositional Analyses of Lunar Pyroclastic Deposits. Icarus 161. 262-280.

Gaskell, R. W., Gillis-Davis, J., Sprague, A. L., 2008. Topography of Mercury from imaging data. In: AAS, Division Planetary Science Meetings 40. Abstract 51.05.

Goudge, T. A., et al., 2014. Global inventory and characterization of pyroclastic deposits on Mercury: new insights into pyroclastic activity from MESSENGER orbital data. J. Geophys. Res. Planets 119, 635-658.

Greeley, R, Batson, R. M., 1990. Planetary Mapping. Cambridge University Press.

Hardy, S., 2015. Does shallow dike intrusion an widening remain a possible mechanism for graben formation on Mars?, Geology 44, 107-110.

Hawke, B. R., Coombs, C. R., Gaddis, L. R., Lucey, P. G., Owensby, P. D., 1989. Remote sensing and geologic studies of localized dark mantle deposits on the Moon. Proc. 19th Lunar Planet. Sci. Conf., 127-135.

Hawkins, S. E. III, et al., 2007. The Mercury Dual Imaging System on the MESSENGER spacecraft, Space Sci. Rev. 131, 247-338.

Head, J. W., 1974. Lunar dark-mantle deposits: possible clues to the distribution of early mare deposits. Proc. Lunar Sci. Conf. 5th, 207-222.

Head, J. W., Wilson, L., 1979. Alphonsus-type dark halo craters: morphology, morphometry and eruption conditions. Proc. 10th Lunar Planet. Sci. Conf., 2861-2897.

Head, J. W., Wilson, L., 1992. Lunar mare volcanism: stratigraphy, eruption conditions, and the evolution of secondary crusts. Geochim. et Cosmochim. Acta 56, 2155-2175.

Head, J. W., Wilson, L., 1993. Lunar graben formation due to near-surface deformation accompanying dike emplacement. Planet. Space Sci. 41, 719-727.

Head, J. W., Wilson, L., Weitz, C. M., 2002. Dark ring in southwestern Orientale Basin: origin as a single pyroclastic eruption. J. of Geophys. Res. 107, E1, 5001.

Head, J. W., et al., 2008. Volcanism on Mercury: Evidence from the first MESSENGER flyby. Science 321, 69-72.

Head, J. W., et al., 2009. Volcanism on Mercury: Evidence from the first MESSENGER flyby for extrusive and explosive activity and the volcanic origin of plains. Earth and Planet. Sci. Lett. 285, 227-242.

Head, J. W., et al., 2011. Flood volcanism in the northern high latitudes of Mercury revealed by MESSENGER. Science 333, 1853-1856.

Head, J. W., Wilson, L., 2017. Generation, ascent, and eruption of magma on the Moon: new insights into source depths, magma supply, intrusions and effusive/explosive eruptions (part 2: predicted emplacement processes and observations). Icaurs 283, 176-223.

Heiken, G. H., McKay, D. S., Brown, R. W., 1974. Lunar deposits of possible pyroclastic origin. Geochim. Cosmochim. Acta 38, 1703-1718.

Hiesinger, H., Head, J. W., Wolf, U., Jaumann, R., Neukum, G., 2011. Ages and stratigraphy of lunar mare basalts: a synthesis. GSA Special Paper 477, 1-51.

Hurwitz, D. M., Head, J. W., Hiesinger, H., 2013. Lunar sinuous rilles: distribution, characteristics, and implications for their origin. Planet. and Space Sci. 79-80, 1-38.

Izenberg, N. R., 2014. The low-iron, reduced surface of Mercury as seen in spectral reflectance by MESSENGER. Icarus 228, 364-374.

Jaupart, C., Vergniolle, S., 1989. The generation and collapse of a foam layer at the roof of a basaltic magma chamber. J. of Fluid Mech. 203, 347-380.

Johnson, A. M., Pollard, D. D., 1973. Mechanics of growth of some laccolithic intrusion in the Henry mountains, Utah, I: field observations, Gilbert's model, physical properties and flow of the magma. Tectonophysics 18, 261-309.

Jolliff, B. L., et al., 2011. Non-mare silicic volcanism on the lunar farside at Compton-Belkovich. Nat. Geosci. 4, 566-571.

Jozwiak, L. M., Head, J. W., Zuber, M. T., Smith, D. E., Neumann, G. A., 2012. Lunar floor-fractured craters: classification, distribution, origin and implications for magmatism and shallow crustal structure. J. Geophys. Res. Planets 117. E11.

Jozwiak, L. M., Head, J. W., Wilson, L., 2015a. Lunar floor-fractured craters as magmatic intrusions: geometry, modes of emplacement, associated tectonic and volcanic features, and implications for gravity anomalies. Icarus 248, 424-447.

Jozwiak, L. M., Head, J. W., Neumann, G. A., Wilson, L., 2015b. The effect of evolving gas distribution on shallow lunar magmatic intrusion density: implications for gravity anomalies. 46th Lunar and Planet. Sci. Conf., Abstract #1580.

Kerber, L., Head, J. W., Solomon, S. C., Murchie, S. L., Blewett, D. T., Wilson, L., 2009. Explosive volcanic eruptions on Mercury: eruption conditions, magma volatile content, and implications for interior volatile abundances. Earth Planet. Sci. Lett. 285, 263-271.

Kerber, L., et al., 2011. The global distribution of pyroclastic deposits on Mercury: the view from MESSENGER flybys 1-3. Planet. and Space Sci. 59, 1895-1909.

Kinczyk, M. J., Prockter, L. M., Chapman, C. R., Susorney, H. C. M., 2016. A morphological evaluation of crater degradation on Mercury: revisiting crater classification with MESSENGER data. Lunar and Planet. Sci. Conf. 47, Abstract #1573.

Klimczak, C., Schultz, R. A., Nahm, A. L., 2010. Evaluation of the origin hypotheses of Pantheon Fossae, central Caloris basin, Mercury. Icarus 209, 262-270.

Klimczak, C., et al., 2013. The role of thrust faults as conduits for volatiles on Mercury. Lunar and Planet. Sci. Conf. 44th, Abstract #1719.

Kreslavsky, M. A., Head , J. W., 2015. A thicker regolith on Mercury. 46th Lunar and Planet. Sci. Conf., Abstract #1832.

Lucchitta, B. K., Schmitt, H. H., 1974. Orange material in the Sulpicius Gallus Formation at the southwestern edge of Mare Serenitatis. Proc. Lunar Sci. Conf. 5th, 223-234.

McClintock, W. E., Lankton, M. R., 2007. the Mercury Atmospheric and Surface Composition Spectrometer for the MESSENGER mission. Space Sci. Rev. 131, 481-521.

Melosh, H. J., McKinnon, W. B., 1988. The tectonics of Mercury. In: Vilas, F., Chapman, C. R., Matthews, M. S. (Eds.), Mercury, U. of Arizona Press, 401-428.

Murchie, S. L., 2008. Geology of the Caloris Basin, Mercury: a view from MESSENGER. Science 321, 73-76.

Ostrach, L. R., et al., 2015. Extent, age, and resurfacing history of the northern smooth plains on Mercury from MESSENGER observations. Icarus 250. 602-622.

Petrycki, J.A., Wilson, L., 1999a. Photographic observations of lunar nearside graben. Lunar Planet. Sci. 30, abstract 1333.

Petrycki, J.A., Wilson, L., 1999b. Volcanic features and age relationships associated with lunar graben. Lunar Planet. Sci. 30, abstract 1335.Prockter, L. M., et al., 2010. Evidence for young volcanism on Mercury from the third MESSENGER flyby. Science 329. 668-671.

Prockter, L. M., et al., 2010. Evidence for young volcanism on Mercury from the Third MESSENGER flyby. Science 329, 668-671.

Prockter, L. M., et al., 2016. The first global geological map of Mercury. Lunar Planet. Sci. Conf. 47th, Abstract #1245.

Robinson, M. S., Lucey, P.G., 1997. Recalibrated Mariner 10 color mosaics: implications for mercurian volcanism. Science 275, 197-200.

Robinson, M. S., et al., 2007. Reflectance and color variations on Mercury: regolith processes and compositional heterogeneity. Science 321, 66-69.

Rothery, D. A., Thomas, R. J., Kerber, L., 2014. Prolonged eruptive history of a compound volcano on Mercury: volcanic and tectonic implications. Earth and Planet. Sci. Lett. 385, 59-67.

Sato, M., 1979. The driving mechanism of lunar pyroclastic eruptions inferred from the oxygen fugacity behavior of Apollo 17 orange glass. Proc. Lunar Planet. Sci. X, 311-325.

Schultz, P. H., 1976. Floor-fractured lunar craters. The Moon 15. 241-273.

Schultz, P. H., 1977. Endogenic modification of impact craters on Mercury, Phy. of Earth and Planet. Interiors 15, 202-219.

Solomon, S. C., 1977. The relationship between crustal tectonics and internal evolution in the Moon and Mercury. Phys. Earth. Planet. Inter. 15, 135-145.

Solomon, S. C., 1978. On volcanism and thermal tectonics on one-plate planets. Geophys. Res. Lett. 5, 461-464.

Solomon, S. C., McNutt, R. L., Gold, R. E., Domingue, D. L., 2007. MESSENGER Mission Overview. Space Sci. Rev. 131, 3-39.

Sparks, R. S. J., 1978. The dynamics of bubble formation and growth in magmas: a review and analysis. J. Volcanol. Geotherm. Res. 3, 1-37.

Spudis, P. D., Guest, J. E., 1988. Stratigraphy and geologic history of Mercury. In: Vilas, F., Chapman, C. R., Matthews, M. S. (Eds.), Mercury, U. of Arizona Press, pp. 118-164.

Squyres, S. W., Janes, D. M., Baer G., Bindschadler, D. L., Schubert, G., Sharpton, V. L., Stofan, E., R., 1992. The morphology and evolution of coronae on Venus. J. Geophys. Res. 97. 13611-13634.

Strom, R. G., Trask, N. J., Guest, J. E., 1975. Tectonism and volcanism on Mercury. J. Geophys. Res. 80, 2478-2507.

Thomas, R. J., Rothery, D. A., Conway, S. J., Anand, M., 2014a. Mechanisms of explosive volcanism on Mercury: implications from its global distribution and morphology. J. Geophys. Res. Planets 119, 2239-2254.

Thomas, R.J., Rothery, D.A., Conway, S.J. and Anand, M., 2014b. Hollows on Mercury: Materials and mechanisms involved in their formation. *Icarus*, *229*, pp.221-235.

Thomas, R. J., Lucchetti, A., Cremonese, G., Rothery, D. A., Massironi, M., Re, C., Conway, S. J., Anand, M., 2015a. A cone on Mercury: analysis of a residual central peak encircled by an explosive volcanic vent. Planet. Space Sci. 108, 108-116.

Thomas, R. J., Rothery, D. A., Conway, S. J., Anand, M., 2015b. Explosive volcanism in complex impact craters on Mercury and the Moon: influence of tectonic regime on depth of magmatic intrusion. Earth and Planet. Sci. Lett. 431, 164-172.

Vergniolle, S., Jaupart, C., 1990. Dynamics of degassing at Kilauea Volcano, Hawaii. J. Geophys. Res. 95, 2793-2809.

Watters, T. R., Schultz, R. A., Robinson, M. A., Cook, A. C., 2002. The mechanical and thermal structure of Mercury's early lithosphere. GRL 29, 37-1 - 37-4 .

Watters, T. R., et al., 2009. Emplacement and tectonic deformation of smooth plains in the Caloris basin, Mercury. Earth and Planet. Sci. Lett. 285, 309-319.

Watters, T. R., et al., 2012. Extension and contraction within volcanically buried impact craters and basins on Mercury. Geology 40, 1123-1126.

Weider, S. Z. et al. (2016) Evidence from MESSENGER for sulfur- and carbon-driven explosive volcanism on Mercury. *GRL*, **43**, 3653–3661.

Weitz, C. M., Head, J. W., Pieters, C. M., 1998. Lunar regional dark mantle deposits: geologic, multispectral, and modeling studies. J. of Geophys. Res. 103, 22525-22759.

Whitten, J. L., Head, J. W., 2015a. Rembrandt impact basin: distinguishing between volcanic and impact-produced plains on Mercury. Icarus 258, 350-365.

Whitten, J. L., Head, J. W., 2015b. Lunar cryptomaria: physical characteristics, distribution, and implications for ancient volcanism. Icaurs 247, 150-171.

Wilhelms, D. E., 1976. Mercurian volcanism questioned. Icarus 28, 551-558.

Wilhelms, D. E., 1987. The geologic history of the Moon. USGS Prof. Paper 1348.

Wilson, L., Head, J. W., 1981. Ascent and eruption of basaltic magma on the Earth and Moon. J. of Geophys. Res. Solid Earth 86, 2971-3001.

Wilson, L., Head, J. W., 2008. Volcanism on Mercury: a new model for the history of magma ascent and eruption. Geophys. Res. Lett. 35, L23205.

Wilson, L., Hawke, B. R., Giguere, T. A., Petrycki, E. R., 2011. An igneous origin for Rima Hyginus and Hyginus crater on the Moon. Icarus 215, 584-595.

Wilson, L., Head, J. W., Tye, A. R., 2014. Lunar regional pyroclastic deposits: evidence for eruption from dikes emplaced into the near-surface crust. 45th Lunar Planet. Sci. Conf., Abstract #1223.

Ziv, A., Rubin, A. M., Agnon, A., 2000. Stability of dike intrusion along preexisting fractures. J. Geophys. Res. 105, 5947-5961.

Zolotov, M. Y., 2011. On the chemistry of mantle and magmatic volatiles on Mercury. Icarus 212, 24-41.

Zuber, M. T., et al., 2012. Topography of the northern hemisphere of Mercury from MESSENGER Laser Altimetry. Science 336, 217-220.

Figure Captions:

Figure 1: The three identification criteria for pyroclastic vents on Mercury. **A**) Physical vent morphology that is distinct from that of a secondary crater. Vent located at 4.4° N, 137.7° W. **B**) A "Red Spot" color anomaly seen in MDIS false-color mosaic (shown here with. R: PC2; G: PC1; B:430/560 nm reflectance. **C**) High reflectance anomaly associated with deposit material. This example is what we term the Rachmaninoff–Copland vent (or the "northeast Rachmaninoff" vent) (35.8° N, 63.8° E) (**B, C**). MDIS monochrome mosaic basemap (**A, C**).

Figure 2: The "simple vent" morphology is characterized by an elongate shape and steep walls sloping to a narrow floor. **A**) An example of the simple vent morphology from Kipling crater (21.1° S, 72.4° E). **B**) An arcuate simple vent, here characterized by several distinct subsidiary vents overlapping to form an overall curved feature. This example is in Picasso crater (3.45° N, 50.4° E). MDIS monochrome mosaic basemap (**A, B**).

Figure 3: The "pit vent" morphology, characterized by approximately equal horizontal dimensions, although the axes are rarely truly equal. Floor profiles are often wider than those of simple vents. **A**) An elliptical pit vent with a bowl-shaped cross-sectional shape, located in Tolstoj basin (21.1° S, 163.02°W). **B**) An irregularly shaped pit vent, called the Rachmaninoff-Copland vent (also called NE Rachmaninoff vent because of its proximity to the Rachmaninoff basin) (35.8° N, 63.8° E). MDIS monochrome mosaic basemap (**A, B**).

Figure 4: The "vent-with-mound" morphology, which is characterized by a central mound surrounded by a wide, annular depression interpreted to be a volcanic vent. **A**) An example of a circular vent-with-mound, situated outside of the Caloris basin at 3.5° S, 136.8° W. The central mound of material is surrounded by a wide, annular depression. The elevation of the central

mound it below that of the surrounding terrain [Thomas et al., 2015]. **B**) An irregularly shaped vent-with-mound example, with a strongly non-circular plan-view shape. The central mound is strongly illuminated and the circumscribing vent is seen entirely in shadow surrounding the mound. The elevation of the central mound is ambiguous; however, the illumination in the above image suggests that the mound height is at least comparable to the elevation of the surrounding terrain, if not elevated above the surrounding region. This vent is located at the northern edge of the Caloris basin (48.7° N, 159.5° E). MDIS monochrome mosaic basemap (**A, B**).

Figure 5: The "shallow pit" morphology is characterized by more than three overlapping, bowl-shaped, circular depressions. It is unclear if this morphology is a primary volcanic feature and it is not included in our catalog. **A**) MDIS image of a "shallow pit" morphology. **B**) MDIS false-color mosaic image of that same feature; note the associated, diffuse, "Red Spot" color anomaly. This example is located at 48.4° S, 6.4° W (image number EN1035095722M) (**A, B**).

Figure 6: Examples of what we term here "irregular pitted terrain", which is characterized by either individual or multiple pits that are irregular in outline and less than 1 km in diameter). Although commonly associated with RS anomalies, it is unclear if this surface texture is a primary volcanic landform; consequently, we do not include such instances in our catalog, although they may be present on vents that we do include. **A**) An example of irregular pitted terrain within the interior of the Rachmaninoff basin (26.2°N, 59.6° E), consisting of multiple pits that have coalesced to form an irregularly textured plain. This region also contains a RS anomaly and a high-reflectance anomaly. Image numbers EN0239705812M and EN0224338598M. **B**) Another instance of irregular pitted terrain located on a simple vent inside the Caloris basin (at 24.3° N, 179° W). Image number EN0258542735M. **C**) An example of "hollows" on Mercury, illustrating the small-scale pitted texture of these landforms. Hollows are

often surrounded by high-reflectance material and are flat-floored. Here, the floor of the crater deGraft is shown (at 22.1° N, 2.02° E); image number EN0250851946M. MDIS monochrome mosaic basemap (**A, B**).

Figure 7: A) Frequency distribution of long axis lengths for both simple vents and pit vents. **B**) Frequency distribution for simple vent long axis lengths. **C**) Frequency distribution for pit vent morphology main axis length. **D**) Frequency distribution of average depth for both simple vents and pit vents.

Figure 8: **A**) The global distribution of pyroclastic vents in our catalog. **B**) The global distribution of pyroclastic vents compared with the distribution of smooth plains deposits on Mercury [after Denevi et al., 2013]. **C**) The global distribution of pyroclastic vents compared with the locations of impact basins greater than 200 km in diameter [Fassett et al., 2011]. The Caloris and Tolstoj basins are labeled C and T, respectively (**A, B, C**) MDIS false-color basemap R: PC2; G: PC1; B:430/560 nm reflectance.

Figure 9: Examples host crater degradation states and the associated inferred mercurian chronostratigraphic period. A) Crater located at 32.4° N, 88.2° E. B) Glinka crater located at 14.9° N, 112.4° W. C) Crater located at 9.45° N, 137.7° W. D) Lermontov crater located at 15.8° N, 48.2° W. E) Tyagaraja crater located at 3.75° N, 148.8° W. MDIS monochrome mosaic basemap, 256 px/deg.

Figure 10: The frequency distribution of inferred host crater ages for simple vents and pit vents. **A**) All examples of these landforms. **B**) Simple vents and pit vents separated by morphologic category. **C**) As for **B**), with vents shown as a percentage of the total mercurian crater population of that degradation class.

Figure 11: The frequency distribution of crater ages (inferred from their degradation states) for vents that do not have an associated RS deposit, plotted as a percentage of the number of vents with that host crater degradation class. Over half of the vents located in craters with a degradation class of 4 (and so corresponding to the Tolstojian period) lack associated RS pyroclastic deposits, attributed to erasure with time due to space weathering and regolith mixing processes.

Figure 12: The length of the long axis for each vent plotted against host crater degradation class.

Figure 13: Three proposed scenarios describing the history of explosive volcanism on Mercury. Scenario 1 describes sustained explosive volcanism throughout mercurian history. Scenario 2 describes two pulses of explosive volcanic history. The initial pulse is centered on 3.7 Ga around the onset of global contraction, and accounts for the formation of all older volcanic vents. The second pulse is centered in relatively recent mercurian history and explains the formation of a few volcanic vents in craters though to have formed in the Mansurian and Kuiperian periods. The dotted line between these two pulses indicates no anticipated explosive volcanic activity in the intervening time. Scenario 3 predicts that the majority of explosive volcanic activity occurred early in mercurian history, tapering off after the transition to a global compressive stress state by about 3.5 Ga. The solid line indicates a continued pattern of explosive volcanic activity through the remainder of mercurian history, albeit at a reduced rate.

Figure 14: Schematic representations of the five candidate formation geometries for mercurian explosive volcanic deposits. **A**) Sill/laccolith formation in the shallow subsurface beneath a crater, leading to uplift of the crater floor and peripheral diking from the edges of the sill. This geometry is based on lunar floor-fractured crater formation geometry [Schultz, 1976; Jozwiak et

al., 2012; 2015]. **B**) Sill/laccolith with dike-tip overshoot model. This geometry is similar to that in **A**, but includes an overshoot of the dike-tip above the upper margin of the sill. This geometry leads to uplift in the crater floor and localizes volcanic morphologies over the dike-tip region. **C**) Surface dike degassing model, characterized by a dike propagating to the surface without interruption and then explosively venting. **D**) Stalled dike degassing model geometry, characterized by a dike stalling at some depth beneath the crater and then degassing, either soon after formation, or after some time of sufficient volatile build-up. **E**) Thrust fault degassing model geometry, wherein a dike propagating from depth intersects an existing thrust fault causing the magma to continue propagation along the thrust fault and explosively vent at the surface along the leading edge of the thrust fault-related landform.

Figure 15: The frequency distribution of vent host crater diameters. The data show no strongly preferred diameter for a crater to host a vent. No vents are observed in craters with diameters less than 20 km, although it is unclear if this is a result of formation mechanism or of data resolution. **A**) All vent host craters we identified. **B**) All vent host craters excluding those greater than 250 km in diameter (i.e. impact basins).

Figure 16: Vent semimajor axis length as a function of host crater diameter. The data show no correlation of these parameters, suggesting that the host crater diameter does not influence the vent formation process. **A**) All host craters in our study. **B**) All host craters excluding those greater than 250 km in diameter (i.e. impact basins).

Figure 17: The vents within Sher Gil crater (D = 73 km, situated at 45.1° S, 134.5° E). The orientations of these four wall-adjacent vents, paired with a lack of observable tectonic deformation of the floor, make the vents in this crater candidate for formation by a deeply-seated

subcrater sill/laccolith. Image numbers EN0251346958M, EN0231267985M, and EN0231267850M.

Figure 18: An example of a single vent within a crater, which could be either the result of a dike tip overshoot or of a stalled/surface dike degassing. This vent is located at 9.45° N, 137.7° W. Image numbers EN0257620579M, EN0242462660M, and EN0212066694M.

Figure 19: An example of a vent located along the leading edge of a thrust fault in the crater 89 km-diameter Glinka (located at 14.9° N, 112.4° W). MDIS monochrome basemap.

Figure 20: An arcuate vent encircling the preserved central peaks of the 100 km-diameter Catullus crater, sitauted at 22° N, 67.5° W. Image number EN1038845919M and MDIS monochrome basemap.

Figure 21: A schematic illustration of the geometric differences between the formation of a simple vent (**A**) and a pit vent (**B**). **A**) During simple vent formation, the dike stalls closer to the surface and produces a relatively narrow, deeper depression. **B**) During pit vent formation, the dike stalls at a greater depth; the resulting infall of material does not reflect as closely as in the first example the underlying dike dimensions, and the result is a less elongated depression than a simple vent.

Figure 22: **A**) Deposit radius as a function of vent length for mercurian vents (blue diamonds) and localized lunar pyroclastic deposits (red squares). A trend line fit to the eight localized lunar pyroclastic deposits shows a close correlation between these two parameters. In contrast, the mercurian data show considerable scatter. **B**) Ejection velocity as a function of vent length for mercurian vents (blue diamonds), localized lunar pyroclastic deposits (red squares), and the Orientale Dark Mantle Ring Deposit (ODMRD) on the Moon (green triangle). A trend line fit to

the localized lunar pyroclastic deposit data shows again a close correlation between vent length and deposit radius. We interpret vents along this line to represent eruptions triggered by foam collapse after the magmatic foam reaches the critical gas volume fraction. This describes all of the localized lunar pyroclastic deposits and a cluster of the mercurian vents. Several mercurian vents are located below this trend line (dashed black ellipse); we interpret this region to represent vents where the original deposit extent has been erased through space weathering and regolith mixing processes. Above the trend line there are numerous mercurian vents, including many small (< 20 km length) vents and the ODMRD. We interpret this region (solid black ellipse) to represent vents where a stalled dike underwent additional volatile build-up processes prior to eruption.

Figure 23: The vents in the crater Picasso show variations in vent degradation correlating with observed pyroclastic deposit extent. The black arrow identifies the northern, less degraded vent, and the white arrow identifies the southern, more degraded vent. **A**) MDIS false color mosaic illustrating the localization of the pyroclastic deposit (characterized by the bright orange color) near the northernmost vent. **B**) MDIS monochrome mosaic of the crater. **C**) MDIS targeted image of the vents, compare the morphological freshness of the northernmost vent (black arrow) with the southernmost vent (white arrow). Image number EN0249929635M.

Figures:

Figure 1

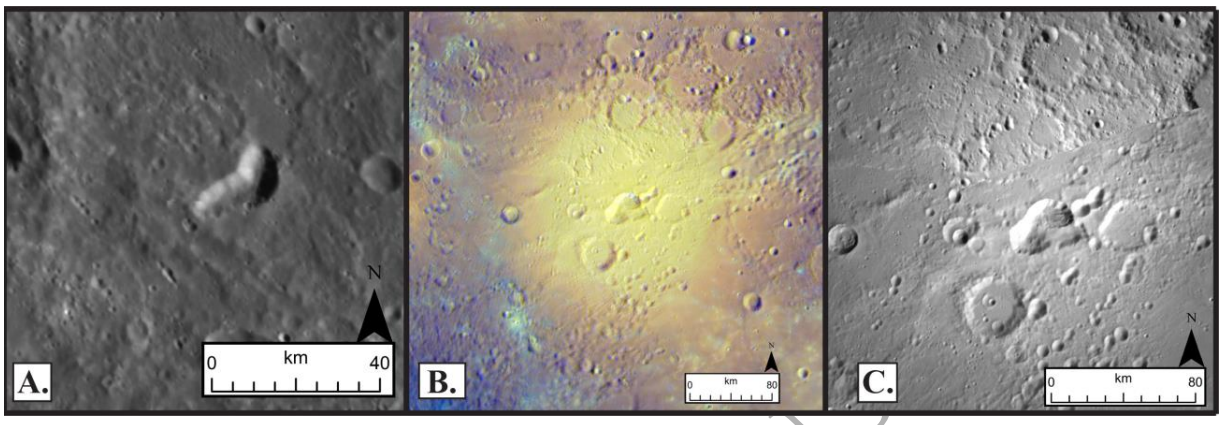

Figure 2

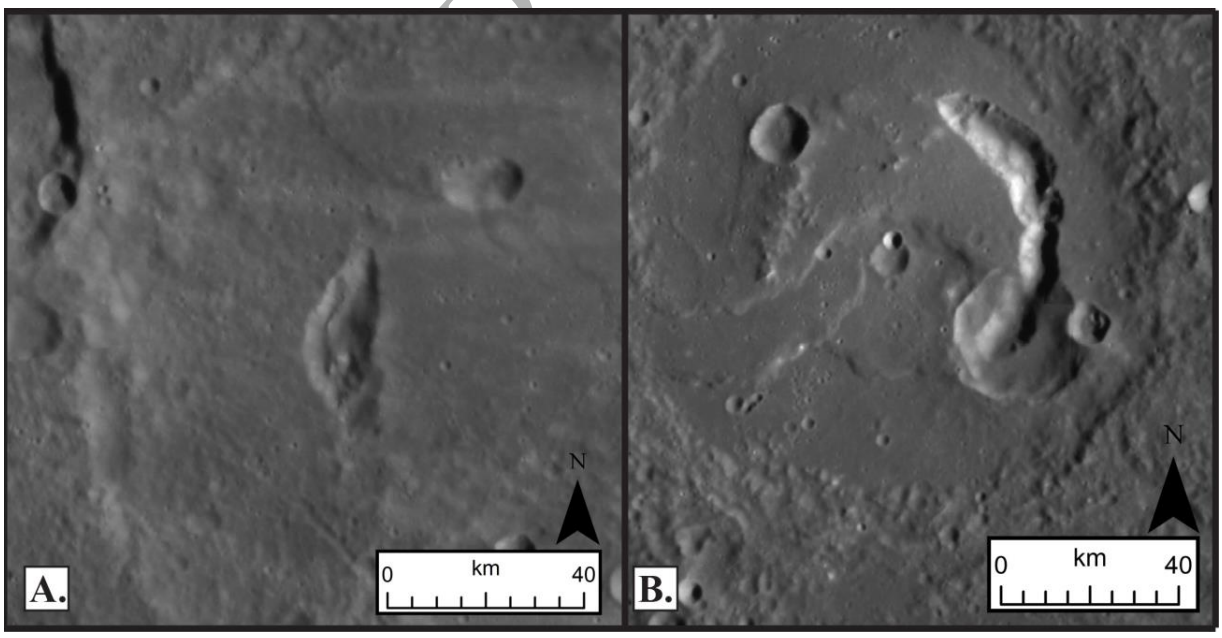

Figure 3

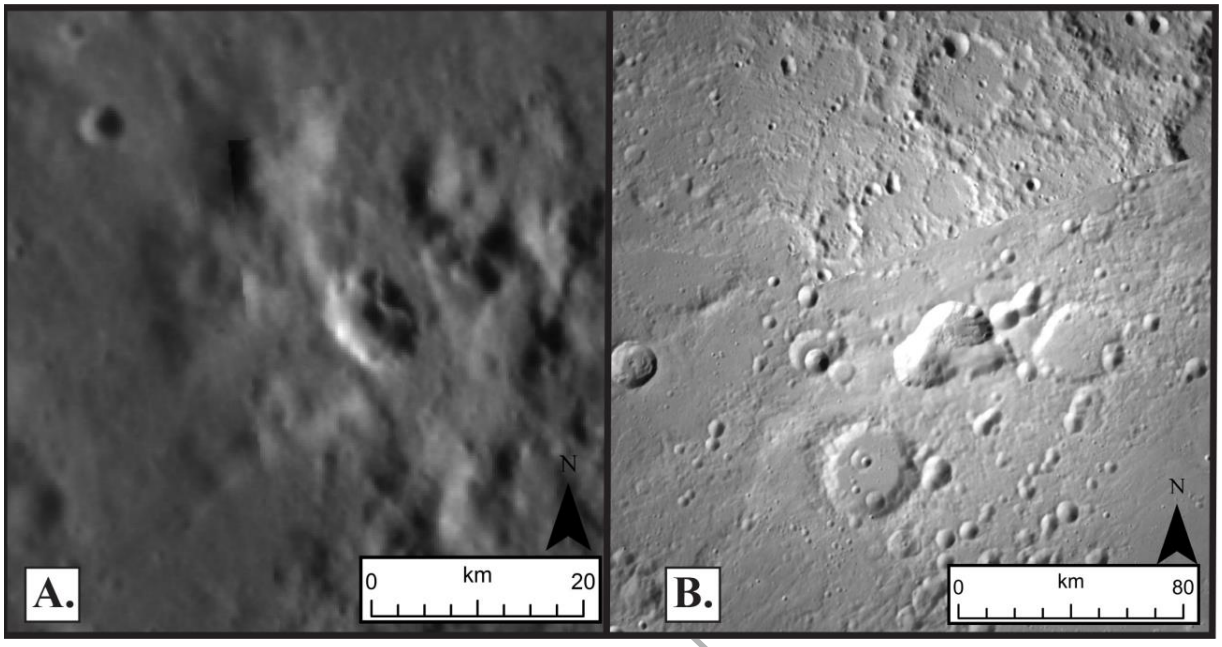

Figure 4

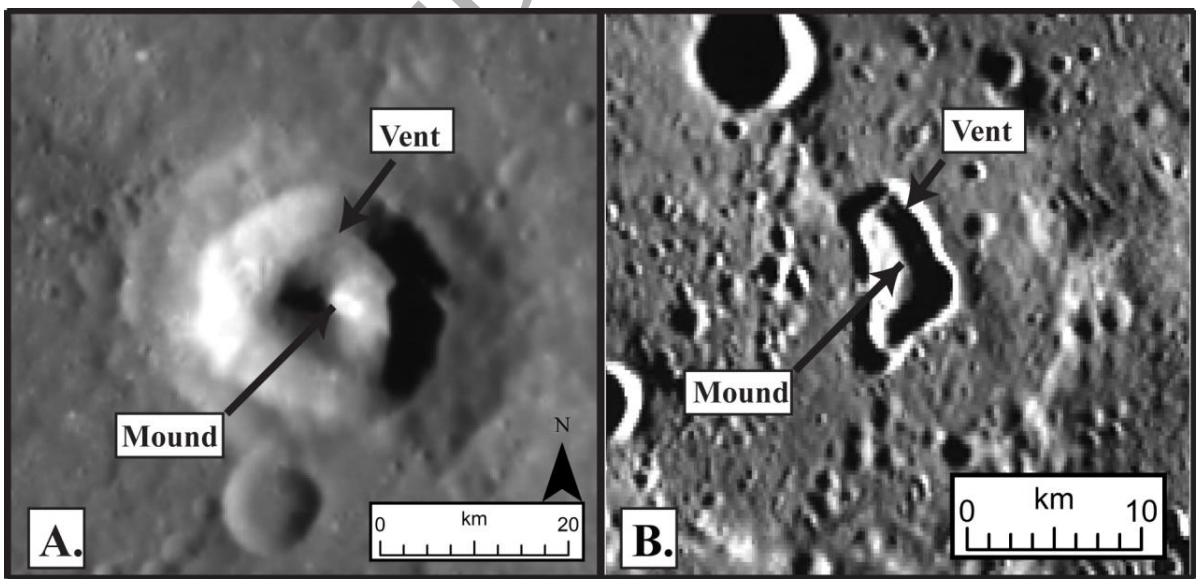

Figure 5

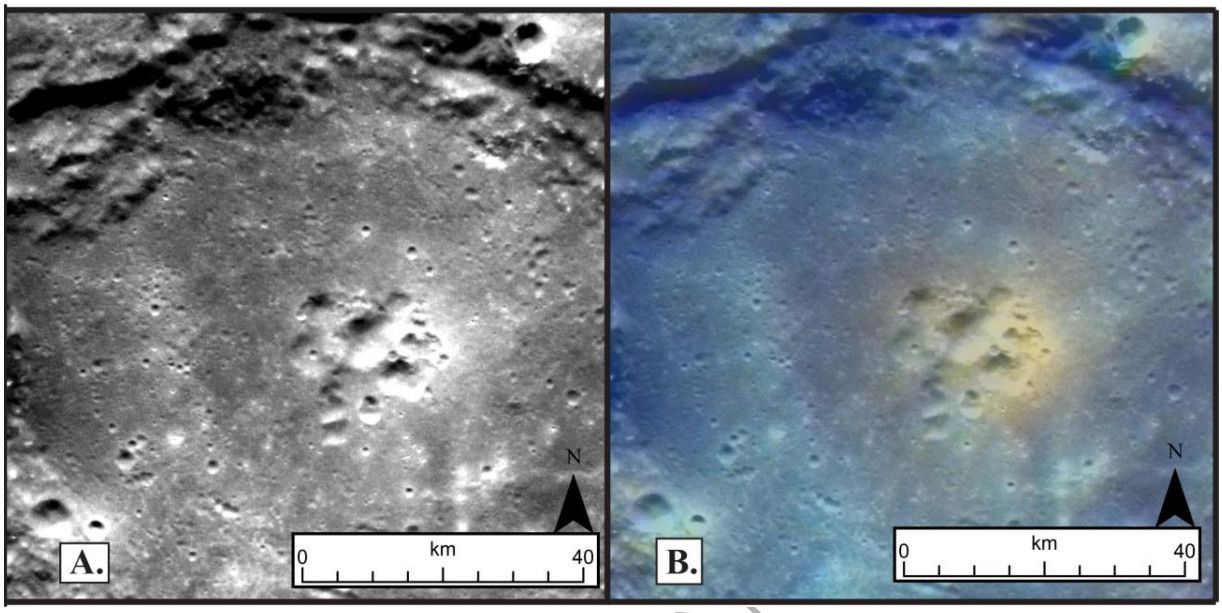

Figure 6

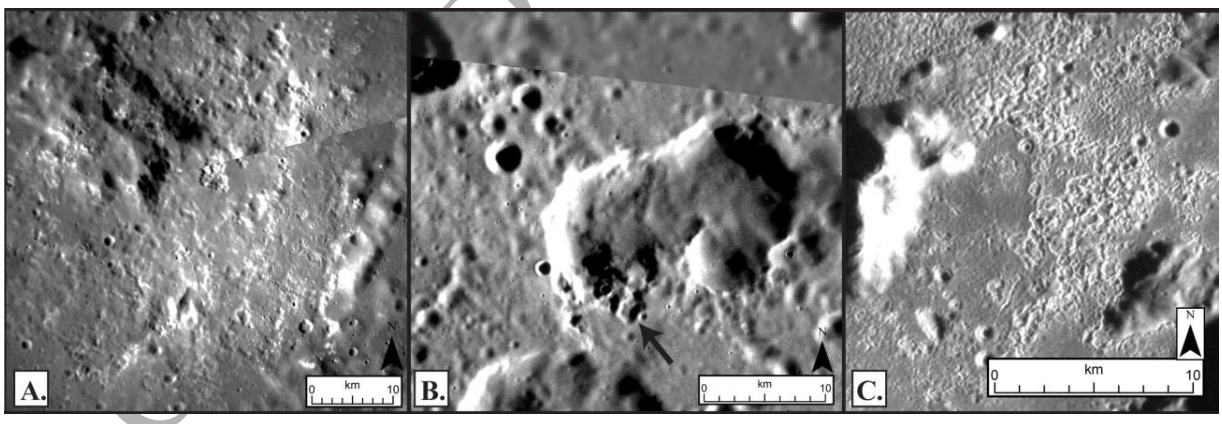

Figure 7

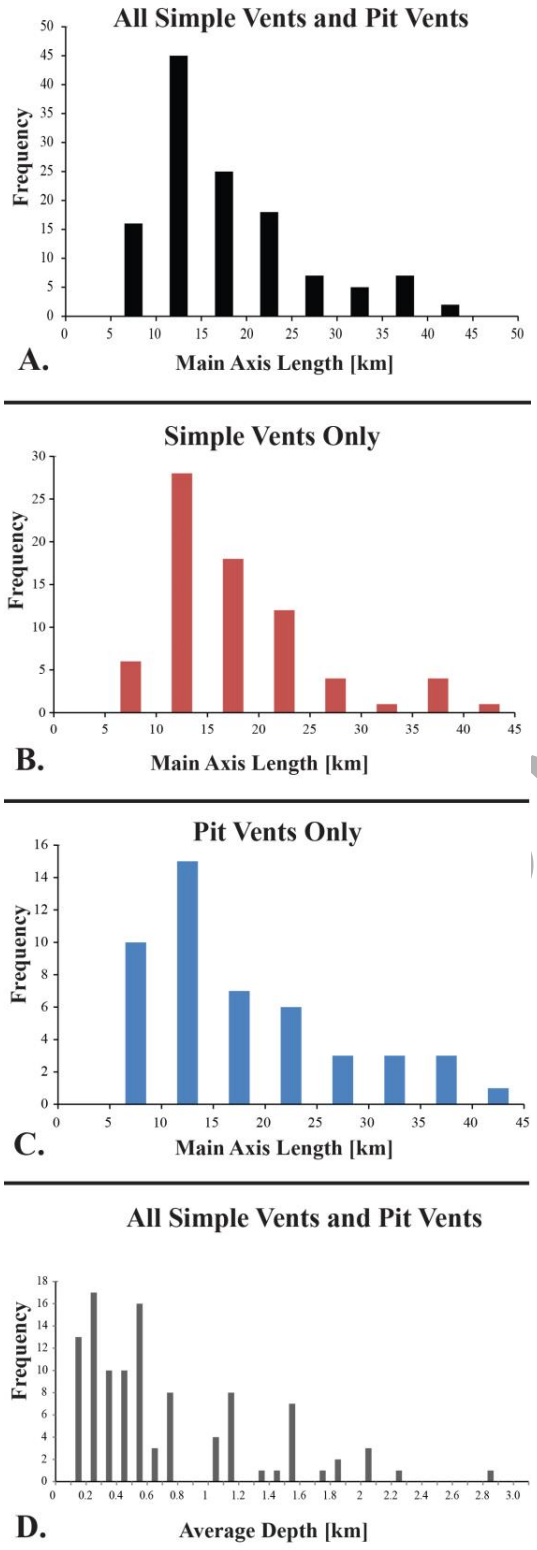

Figure 8

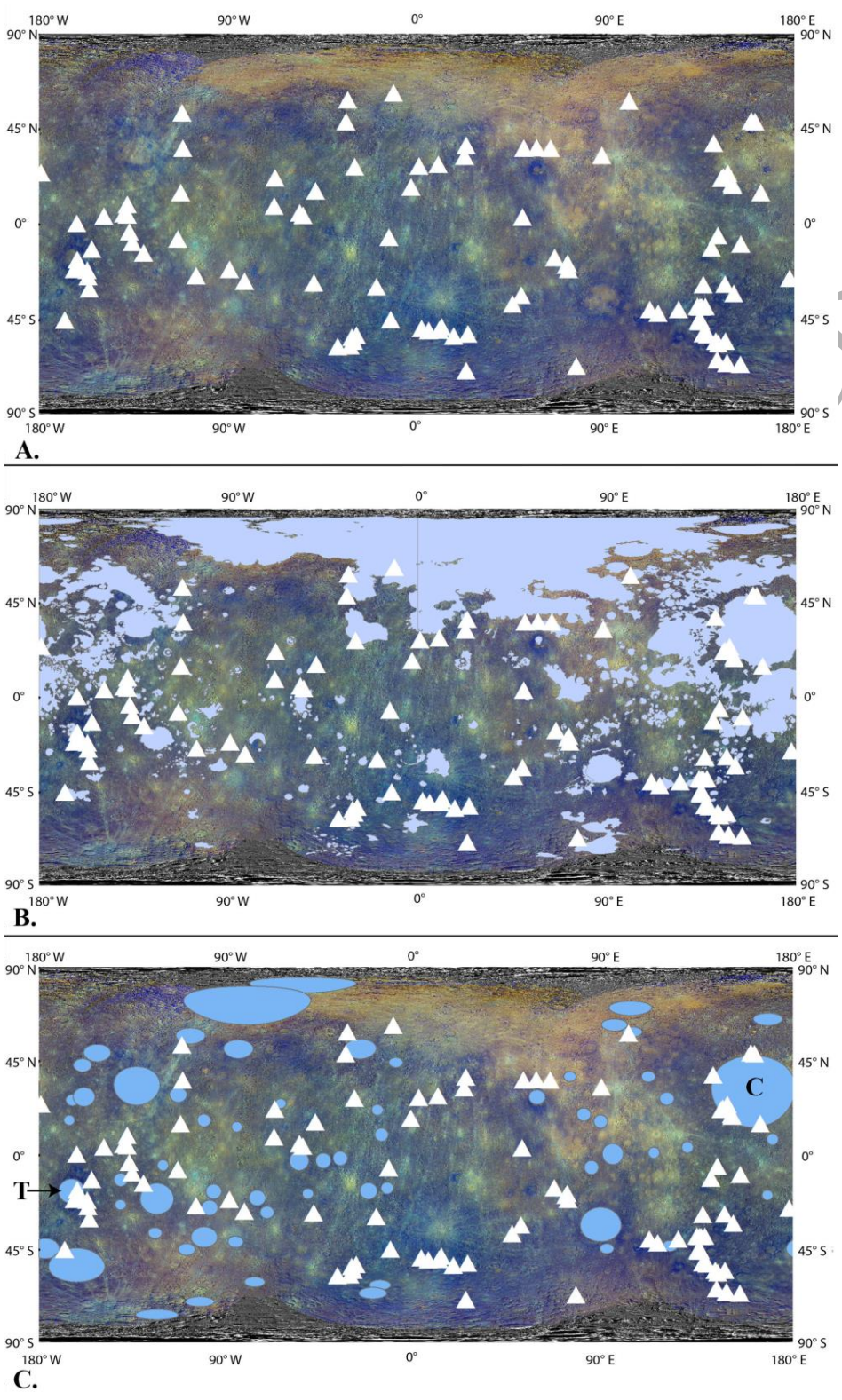

Figure 9

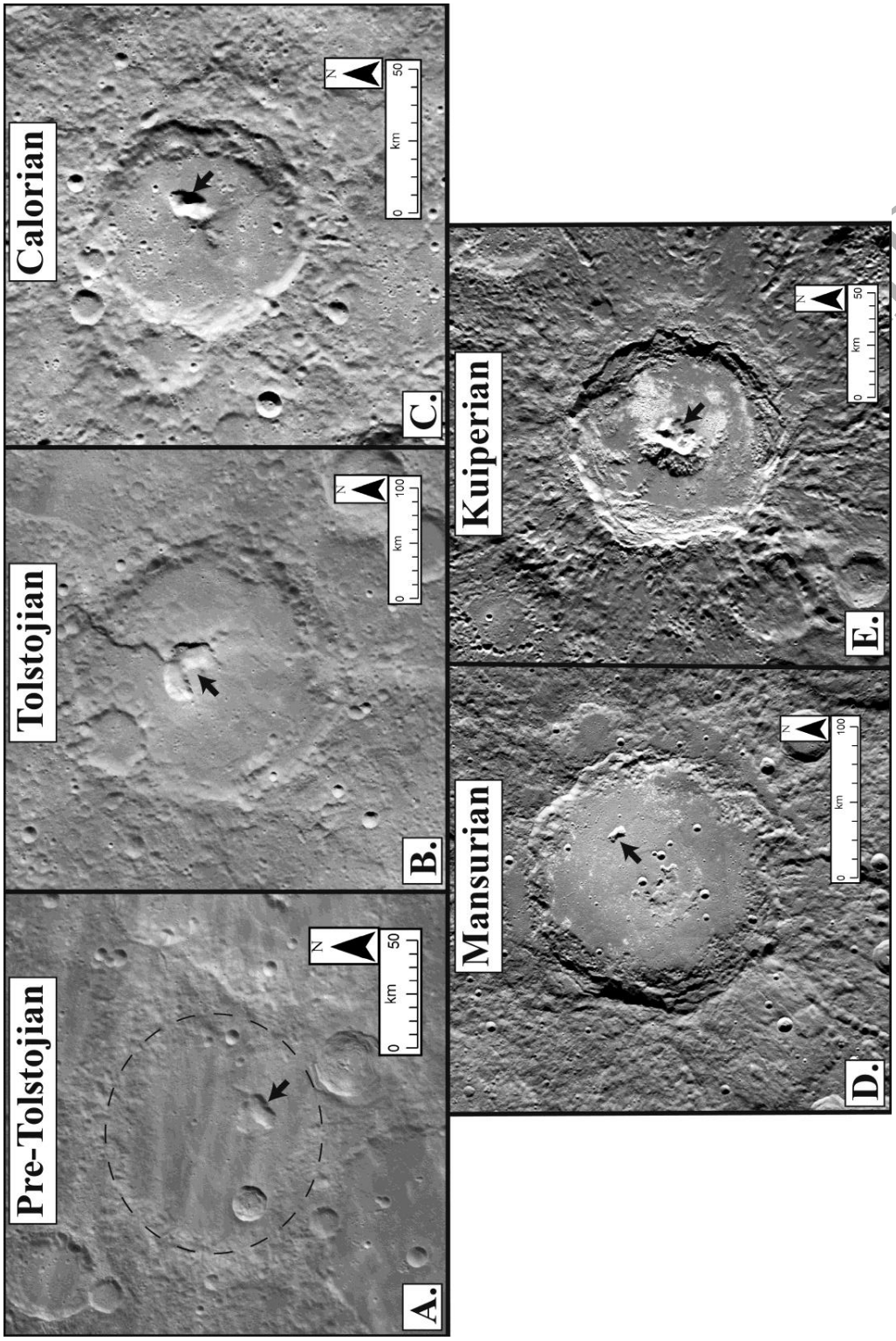
Pre-Tolstojian
A.
Tolstojian
B.
Calorian
C.
Mansurian
D.
Kuiperian
E.
N
km
0
50
100

Figure 10

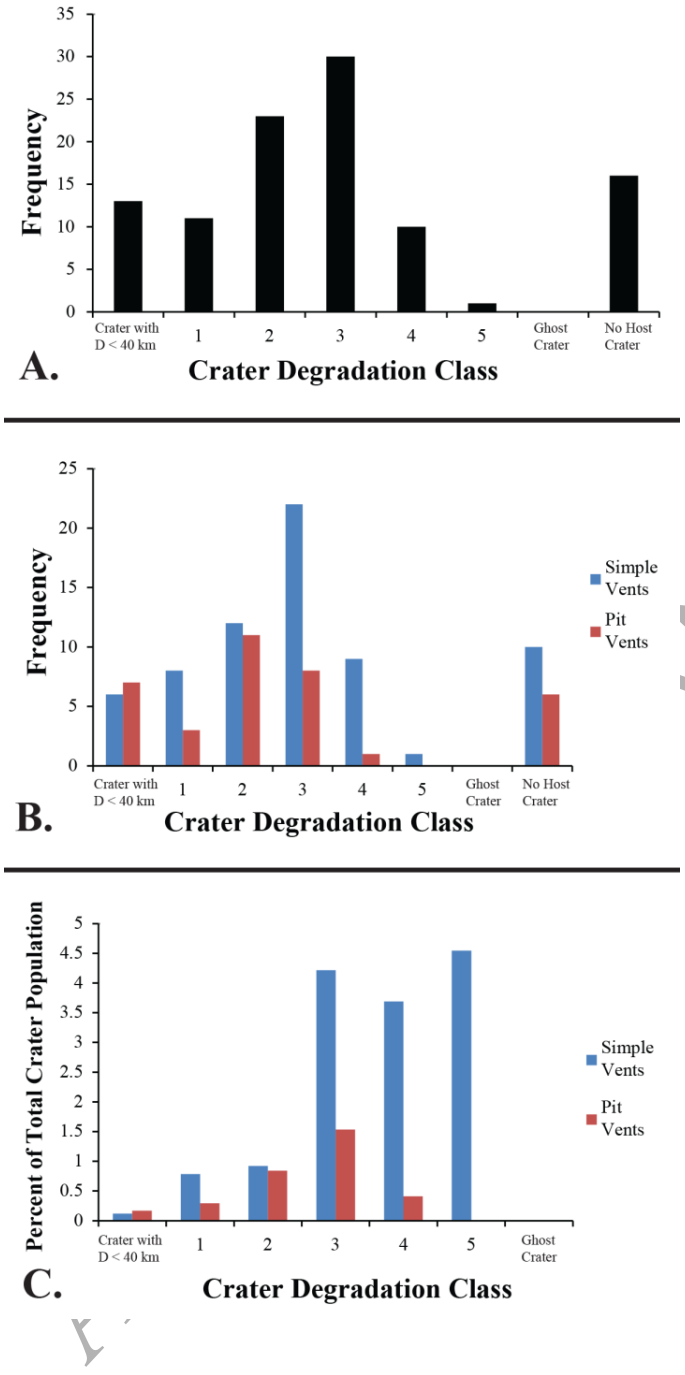

Figure 11

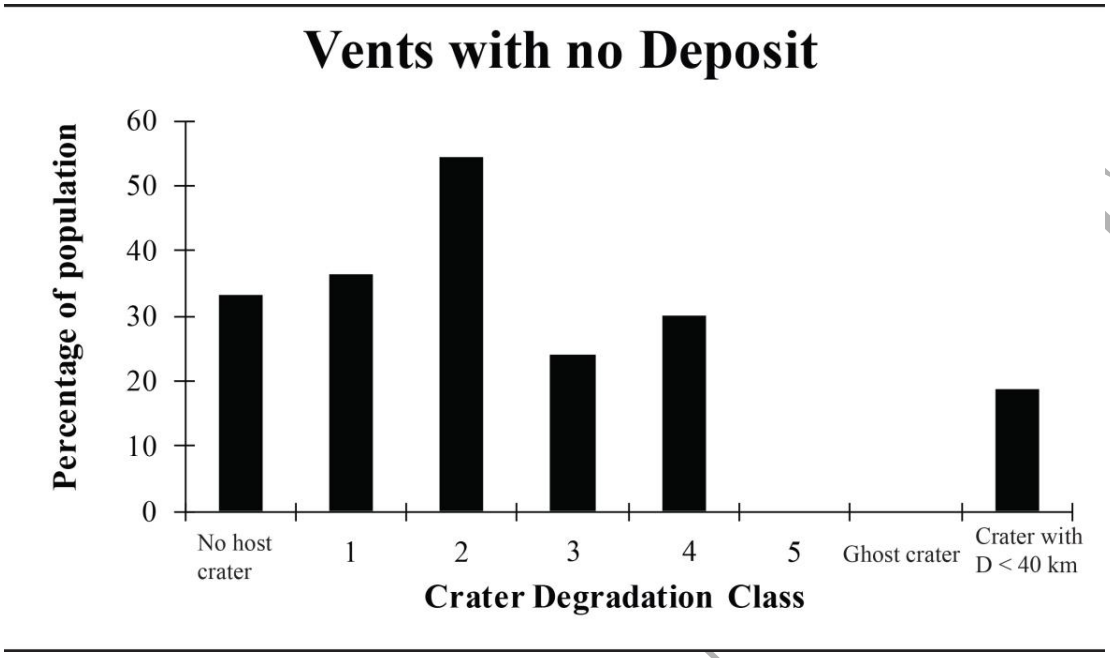

Figure 12

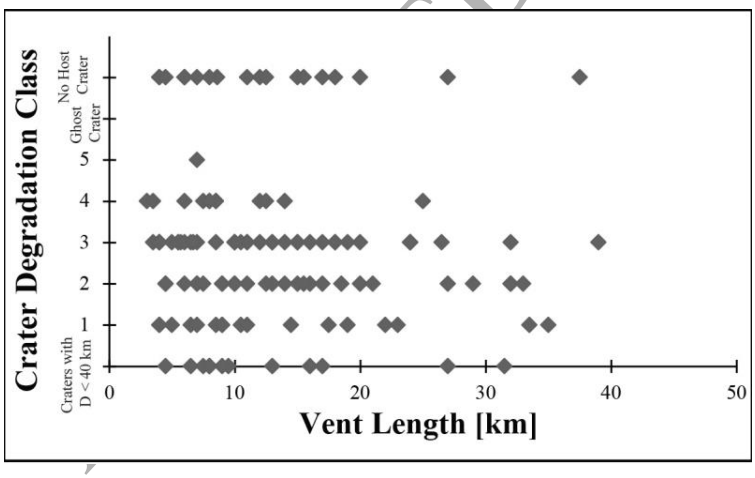

Figure 13

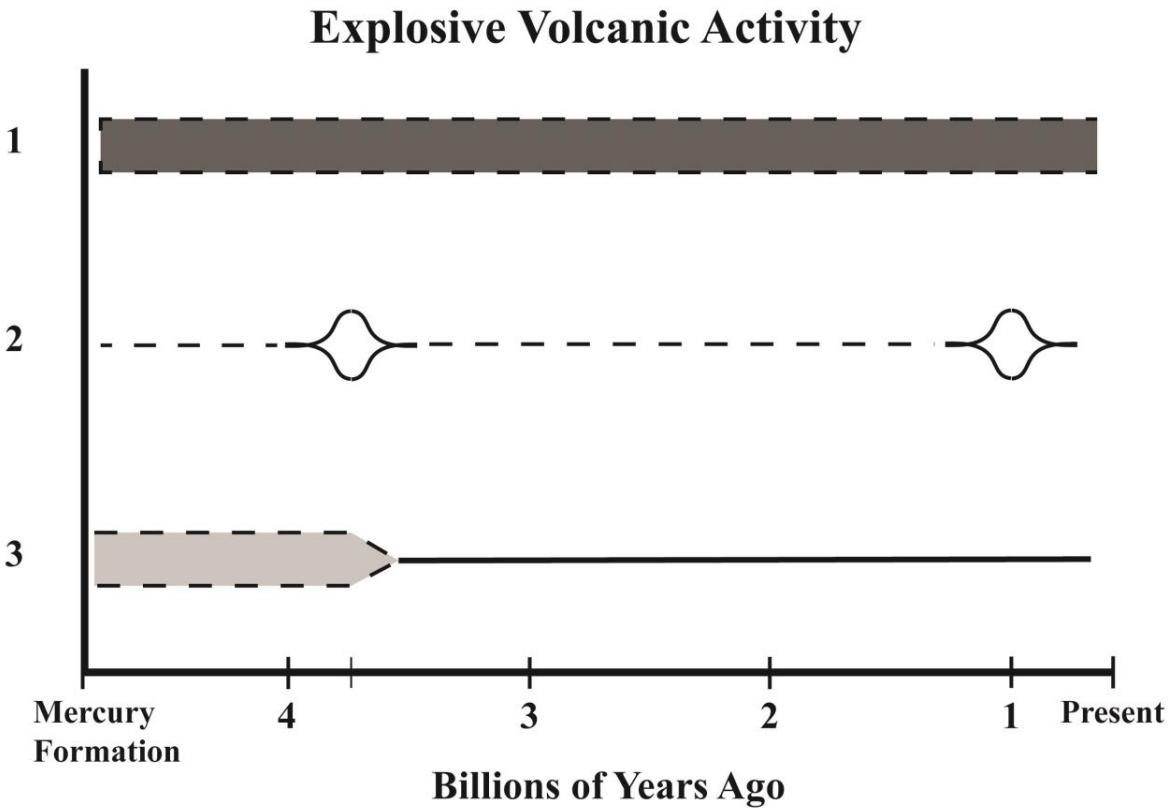

Figure 14

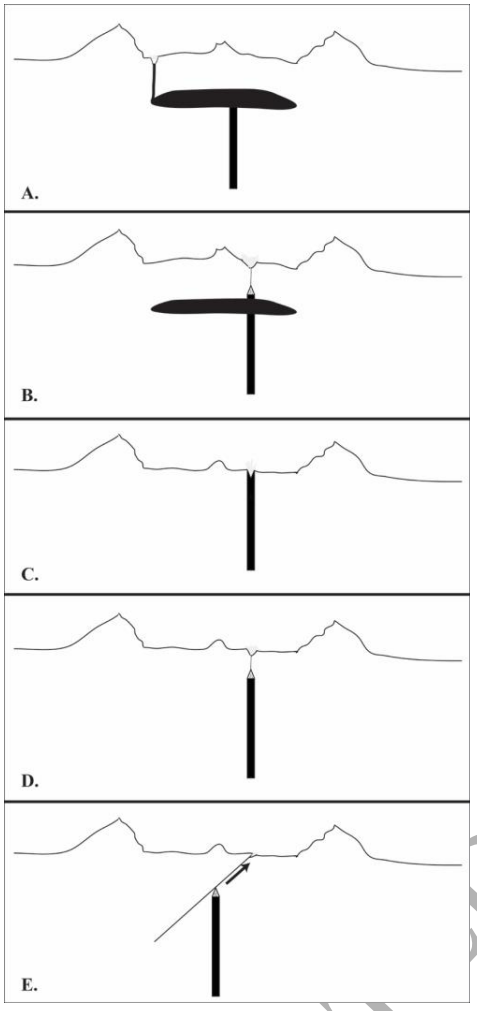

Figure 15

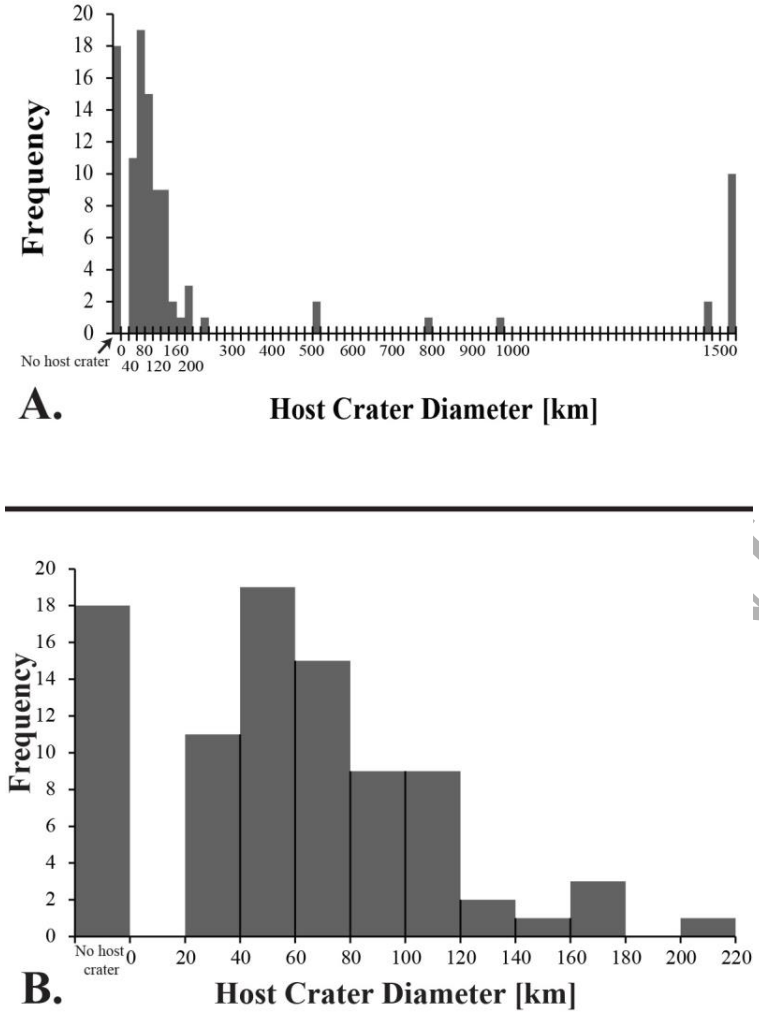

Figure 16

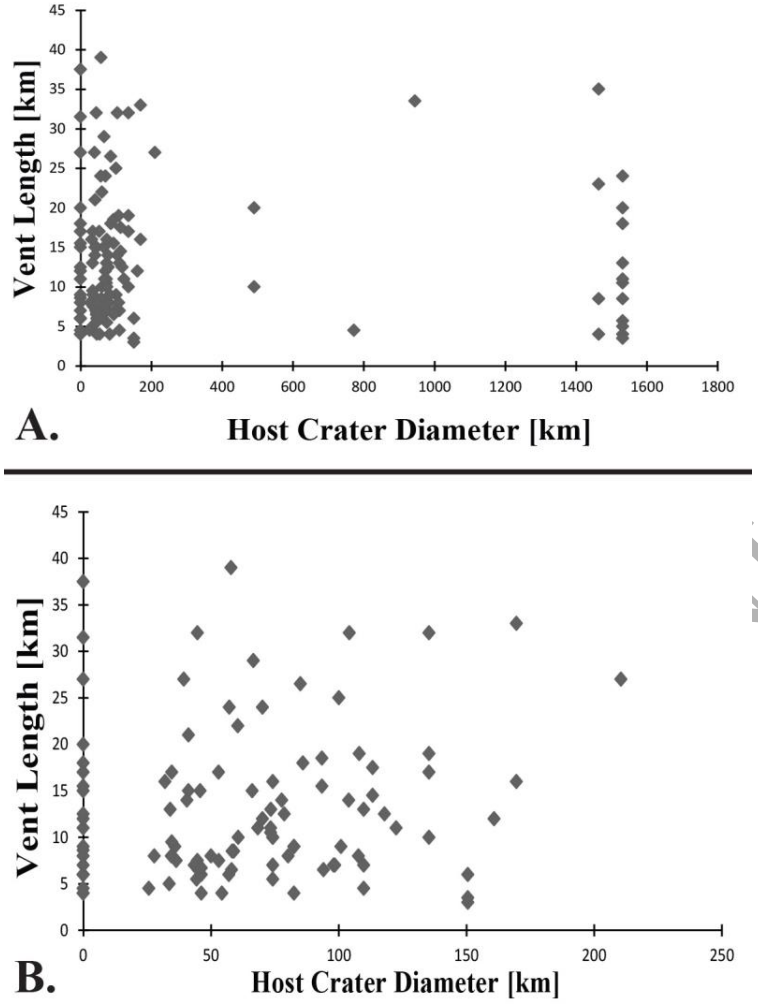

Figure 17

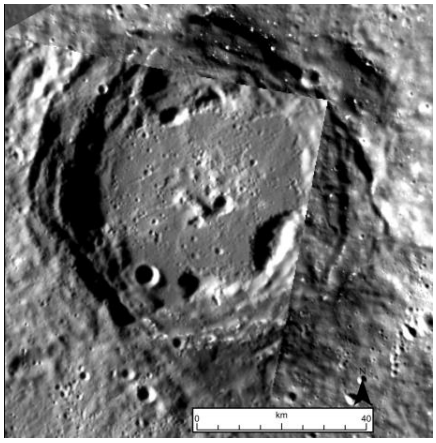

Figure 18

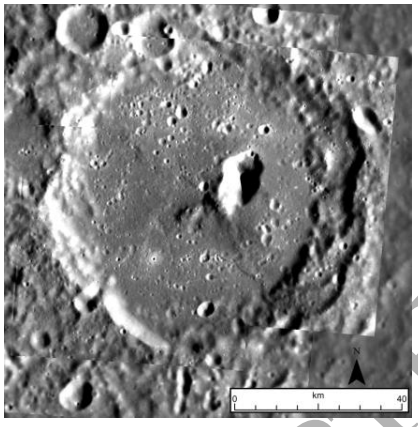

Figure 19

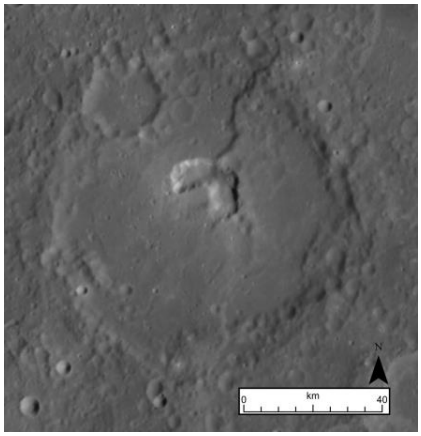

Figure 20

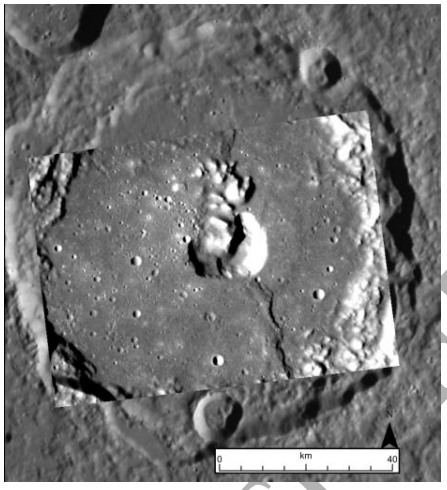

Figure 21

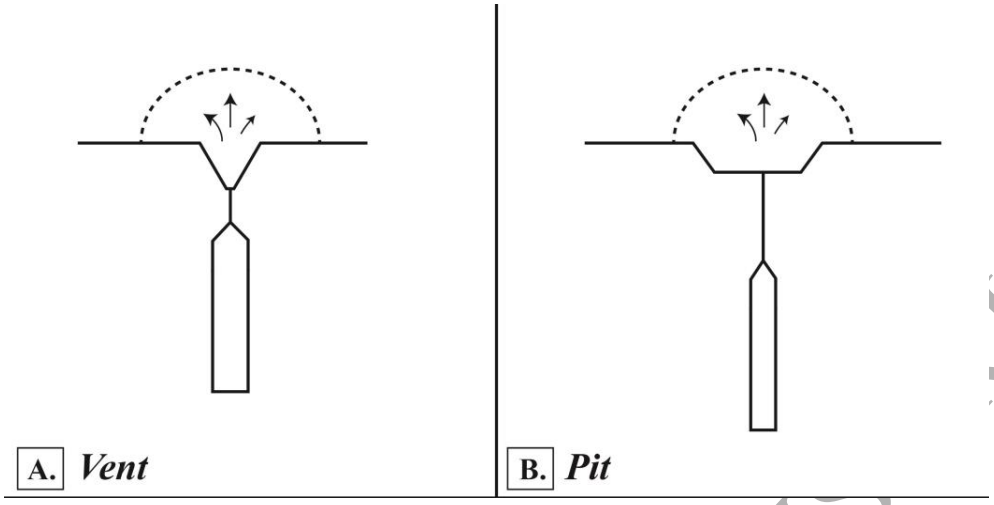

Figure 22

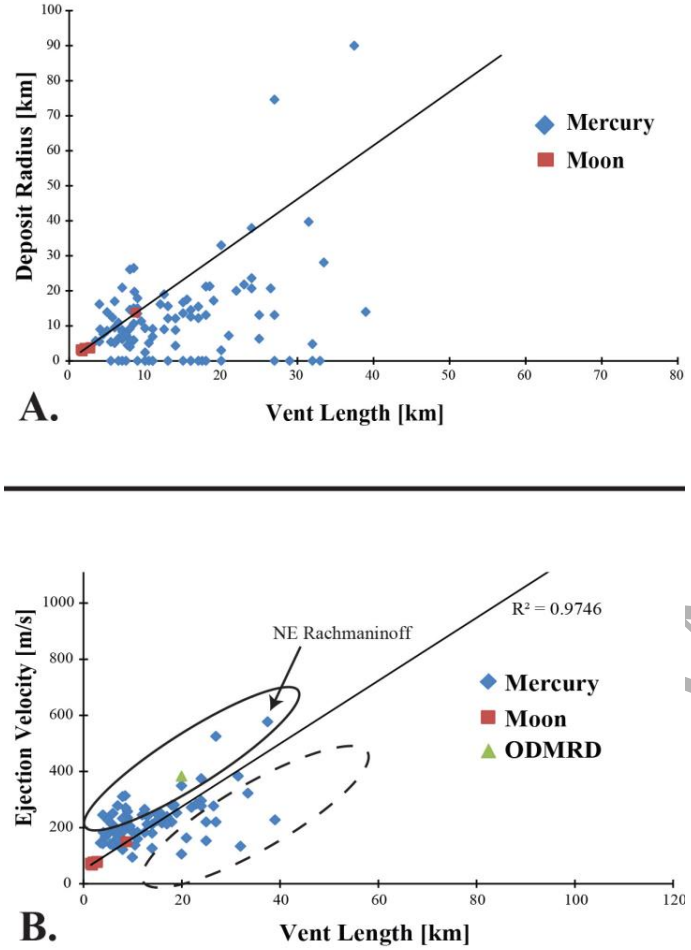

Figure 23

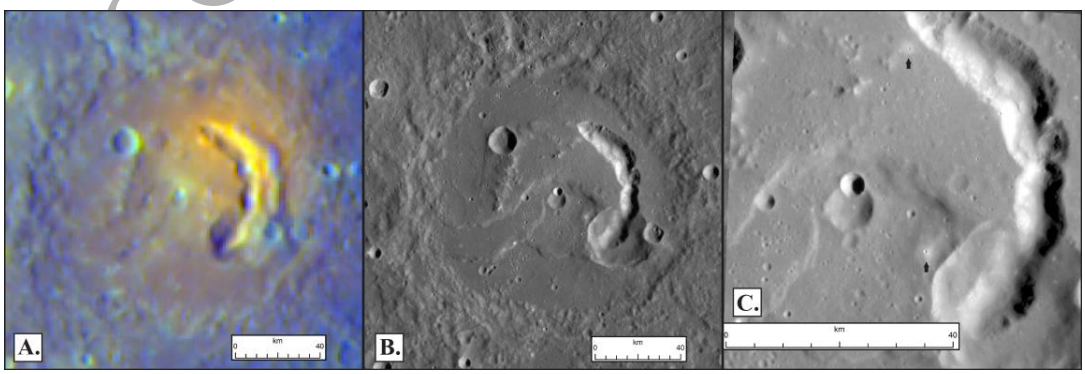

Table 1: Candidate Pyroclastic Vents

Crater Name[1]	**Center Longitude**[2]	**Center Latitude**	**Host Crater Diameter [km]**	**Degradation Class**[3]	**Morphology classification**
RS-05 (K2)	-179	24.3	1532	3	Simple Vent
Unnamed crater 8 (G11)	-167.6	-45.04	34.1	N/C	Simple Vent
Tolstoj S (G6)	-163.02	-21.13	490.5	2	Pit Vent
Unnamed crater 4 (K36)	-161.9	0.5	60.7	2	Pit Vent
Tolstoj E (G5)	-161.7	-16.7	490.5	2	Simple Vent
Tolstoj SE (G7)	-161.14	-19.88	34.5	2	Pit Vent
Eitoku	-156.926	-21.6354	104	2	Simple Vent
	-156.461	-24.6265	50	4	Simple Vent
	-155.945	-30.3481	98.5	1	Simple Vent
	-154.646	-11.7315	54.3	3	Pit Vent
Tyagaraja (G8)	-148.88	3.75	98	5	Simple Vent
	-139.488	5.08245	57	2	Simple Vent

	-137.787	4.43584	0	-	Simple Vent
	-137.764	9.45622	73.5	3	Simple Vent
	-136.788	-3.54144	39.4	N/C	VwM
	-135.493	-8.41149	60.5	1	VwM
	-129.994	-13.5333	94.1	3	Simple Vent
	-113.785	-6.93635	66.2	3	VwM
Glinka (K29)	-112.4	14.9	93.5	2	Simple Vent
To Ngoc Van (K10)	-111.8	52.6	70.2	3	Pit Vent
Gibran (K15)	-111.3	35.8	104.2	2	Pit Vent
Rumi	-105.024	-24.1346	78.7	2	Pit Vent
	-89.2117	-21.2196	57.2	3	Pit Vent
	-81.9273	-26.7598	(944.7)[4]	-	Simple Vent
	-67.9205	8.59485	21.4	N/C	Pit Vent
Unnamed crater 1 (K26)	-67.5	22	100.1	4	Simple Vent
Mistral NW	-55.8	5.4	45.8	3	Simple Vent

(K33)					
Mistral SE (K18)	-54.2	4.2	100.9	2	Simple Vent
	-48.9	-27.5	0	-	Pit Vent
Lermontov NE (K7)	-48.2	15.8	160.9	4	Simple Vent
Kuniyosi	-37.5289	-57.6204	25.7	N/C	Simple Vent
Enheduanna (K22)	-33.7	48.4	108.1	2	Pit Vent
Unnamed crater 6 (G9)	-32.9	58.8	32	N/C	Simple Vent
Hesiod a (K4)	-31.7	-57.2	91.3	2	Pit Vent
Hesiod c (K13)	-30.9	-53.2	33.7	N/C	Pit Vent
Hesiod b (K14)	-30	-55	0	-	Pit Vent
Geddes (K16)	-29.5	27.2	85	3	Pit Vent
Hesiod d (K32)	-28.6	-52.2	0	-	Simple Vent
	-19.1131	-29.4306	0	-	VwM
	-13.0714	-6.06093	68.4	2	Pit Vent

Rilke	-12.4139	-44.78	77.7	4	Simple Vent
Abedin	-10.9485	61.8274	118	4	Simple Vent
Hemingway (K3)	-2.7	17.6	122.5	3	SimpleVent
	1.19122	27.5251	772.3	0	Simple Vent
	2.26688	-48.9564	0	-	Simple Vent
	5.80077	-50.0023	0	-	Simple Vent
	10.2985	28.3662	$(1392)^5$	-	Simple Vent
	10.7517	-49.8341	0	-	Simple Vent
	11.8058	-48.3247	0	-	Simple Vent
	17.7142	-52.7133	0	-	Simple Vent
	22.7546	32.1695	$(1392)^5$	-	Simple Vent
	23.67	37.33	0	-	Simple Vent
	23.6707	-68.8936	0	-	Pit Vent
	24.4144	-51.6599	58.9	4	Simple Vent
	45.6213	-37.5026	58.3	4	Simple Vent
	49.9534	-33.261	$(1445.5)^6$	-	Pit Vent

Picasso (K37)	50.4	3.45	135.4	3	Simple Vent
	51.1418	35.9417	27.8	N/C	Simple Vent
N Rachmaninoff (G4)	57.3	36.1	0	-	Pit Vent
NE Rachmaninoff (K1)	63.8	35.8	0	-	Pit Vent
	65.7418	-15.563	$(1445.5)^6$	-	Simple Vent
Kipling W (G2)	71.43	-19.21	169.6	2	Simple Vent
Kipling N (G1)	72.03	-18.45	169.6	2	Simple Vent
Kipling S (G3)	72.4	-21.16	86	3	VwM
Alver	76.16	-66.78	150.56	4	Pit Vent
Unnamed crater 7 (G10)	88.2	32.4	113.3	1	Simple Vent
	101.077	58.2096	210.5	2	Pit Vent
Beckett (K34)	111.2	-40	57.9	3	Simple Vent
	115.104	-41.9784	53.02	2	Pit Vent

	124.806	-40.0887	40.6	3	Simple Vent
	133.703	-38.6423	35.9	N/C	Pit Vent
Sher Gil SW	134.4	-45.7	74.2	3	Simple Vent
Sher Gil NW	134.65	-44.8	74.2	3	Simple Vent
Sher Gil S	134.8	-45.78	74.2	3	Simple Vent
	134.95	-38.93	43.5	2	Pit Vent
Sher Gil N	135	-44.7	74.2	3	Simple Vent
Sher Gil SE	135.45	-45.54	74.2	3	Simple Vent
	135.69	-38.87	44.7	2	Pit Vent
	136.546	-51.5263	25.9	N/C	Simple Vent
	136.61	-28.28	46.2	3	Simple Vent
	137.633	-38.6292	36.4	N/C	Pit Vent
Unnamed crater 5a (K38)	138.6	-52	80.2	4	Simple Vent
	140.58	-11.0137	66.6	2	Simple Vent
Caloris	141.471	38.2797	1532	3	Pit Vent
Unnamed crater	142.5	-55.1	41.2	2	Simple Vent

5b (K39)					
	143.04	-63.85		2	Simple Vent
	143.593	-5.20355	82.5	2	Pit Vent
Unnamed crater 5c (K40)	143.8	-56.2	0	-	Pit Vent
Caloris RS-03 SE (K28)	145.4	21.7	1532	3	Pit Vent
Caloris RS-03 (K5)	146.2	22.3	1532	3	VwM
	146.868	-28.2183	53.1	4	Simple Vent
	147.151	-55.0409	44.4	3	Simple Vent
	147.64	-65.52	34.7	N/C	Pit Vent
	147.86	-65.15	34.7	N/C	Pit Vent
Caloris	148.383	24.2069	1532	3	Pit Vent
Caloris RS-03 SE (K35)	150.2	19.4	1532	3	Simple Vent
Caloris	150.5	18.6	1532	3	Simple Vent
	151.114	-32.5761	58.1	1	Simple Vent

	154.247	-65.9282	44.7	2	Pit Vent
	154.509	-9.21725	73.4	1	Simple Vent
Caloris	159.48	48.6929	1532	3	VwM
Caloris	161.229	48.4023	1532	3	VwM
Caloris RS-04d (K27)	164	15	1532	3	Pit Vent
	177.767	-25.3508	109.8	2	Simple Vent

[1]Crater names are listed for all craters with IAU-approved names. Unnamed craters identified in Kerber et al. [2011] and Goudge et al. [2014] are designated with (K) and (G), respectively, and maintain the designation from the original work for ease of comparison. Craters and locations with neither a formal name nor an informally applied name from previous works are left blank.

[2]East-positive longitude values.

[3]Crater degradation class from Kinczyk et al. [2016]. Class 1: most degraded; Class 5: least degraded. The designation "N/C" indicates a vent located in a crater with diameter < 40 km and no associated crater degradation class. The designation " - " indicates a vent with no associated host crater.

[4] Probable basin Matisse-Repin (Fassett et al., 2012).

[5] Probable basin b30 (Fassett et al., 2012).

[6] Suggested, but unverified basin b56 (Fassett et al., 2012).

Table 2: Catalog of Shallow Pit morphologies

Crater Name[1]	Center Longitude[2]	Center Latitude	Host Crater Diameter [km]	Degradation Class[3]	Morphology classification
	-104.822	-22.0732	-	1	Shallow Pits
Kuniyoshi	-37.5289	-57.6204	26.5	0	Shallow Pits
	-6.4235	-48.4267	119.5	4	Shallow Pits
	13.0063	-70.6439	119.6	3	Shallow Pits
	20.171	-53.0162	-	-	Shallow Pits
	24.16	37.4	-	-	Shallow Pits
	141.492	-59.6059	-	-	Shallow Pits
	147.44	-65.28	35	0	Shallow Pits
Liang Kai	175.655	-39.7556	144.9	2	Shallow Pits
	177.55	-24.96	103.6	2	Shallow Pits

[1]Crater names are listed for all craters with IAU-approved names. Unnamed craters identified in Kerber et al. [2011] and Goudge et al. [2014] are designated with (K) and (G), respectively, and maintain the designation from the original work for ease of comparison. Craters and locations with neither a formal name nor an informally applied name from previous works are left blank.

[2]East-positive longitude values.

[3]Crater degradation class from Kinczyk et al. [2016]. Class 1: most degraded; Class 5: least degraded.

Table 3: Catalog of Irregular Pitted Terrain locations

Crater Name[1]	Center Longitude[2]	Center Latitude	Host Crater Diameter [km]	Degradation Class[3]	Morphology classification
Caloris	-178.97	24.2694	1532	-	IPT
Tolstoj	-163.391	-20.2439	390	2	IPT
Zeami	-147.242	-2.9716	128.5	4	IPT
Scarlatti	-100.813	41.1319	131.9	3	IPT
	-98.5088	42.0109	-	0	IPT
	-90.5563	-22.8582	68.1	3	IPT
	-90.5563	-22.8582	68.6	3	IPT
Raphael (K8)	-74.4	-21	342.1	2	IPT
	-67.9205	8.59485	20	0	IPT
Chekhov	-61.7467	-37.264	193.8	2	IPT
Praxiteles	-59.4069	26.6068	198.1	3	BIP
	-56.085	3.7557	38.5	0	IPT
Mistral	-54.0909	4.18191	101.9	2	IPT
Chaikovskij	-51.3424	7.47479	171.01	2	IPT
Lermontov	-49.0076	15.0086	165.8	4	IPT
	-44.2048	12.1812	-	1	IPT
Enheduanna	-33.9994	48.3288	105	2	IPT
Namatjira	-32.8942	58.8416	34	0	IPT
Hesiod	-31.6951	-58.0857	101.03	2	IPT
Hesiod c (K13)	-30.9	-53.2	94.4	0	IPT
Hesiod b (K14)	-30	-55	-	-	IPT
Geddes	-29.5	26.78	83.5	3	IPT
Hesiod e (K24)	-27.9	-51.5	37.4	0	IPT
	-6.04293	-47.0739	120.8	4	IPT
Melville	-4.2	26.2	39.4	1	IPT
	1.19122	27.5251	18.3	0	IPT
	21.75	32.42	25.3	0	IPT
	23.1669	35.5111	76.1	3	IPT
	24.15	37.44	-	-	IPT
Donelaitis	38.2961	-52.8102	84.5	4	IPT
	55.2924	36.3165	20.1	0	IPT
Rachmaninoff SE (K17)	59.8	26.2	305.6	4	IPT
	100.55	58.25	-	2	IPT
Beckett	111.336	-40.3069	60.2	3	IPT
	115.104	-41.9784	52.2	2	IPT
Sher Gil center	135.03	-45.17	81.4	3	IPT
	140.046	-52.28	84.9	4	IPT

	142.22	-35.16	101.2	2	IPT
	142.317	-55.22	42	2	IPT
	142.665	-63.5287	86.1	2	IPT
Moody	144.9	-13.3	82.6	4	IPT
	145.26	-59.833	53.5	2	IPT
	146.88	-55.24	43.2	3	IPT
Caloris	148.147	18.535	1532	3	IPT
Caloris	150.557	46.8633	1532	3	IPT
Caloris	152.572	17.6497	1532	3	IPT
Caloris RS-04b (K20)	156.9	16.7	1532	3	IPT
Caloris RS-04a (K21)	159.2	14.1	1532	3	IPT
Navoi	160.686	58.8242	68.6	3	IPT
Caloris RS-04c (K23)	162.1	14.2	1532	3	IPT
Caloris	162.362	13.7039	1532	3	IPT
	168.064	60.8055	66.9	3	IPT
Caloris	179.461	23.0499	1532	0	IPT
	179.722	-23.6502	-	4	IPT

[1]Crater names are listed for all craters with IAU-approved names. Unnamed craters identified in Kerber et al. [2011] and Goudge et al. [2014] are designated with (K) and (G), respectively, and maintain the designation from the original work for ease of comparison. Craters and locations with neither a formal name nor an informally applied name from previous works are left blank.

[2]East-positive longitude values.

[3]Crater degradation class from Kinczyk et al. [2016]. Class 1: most degraded; Class 5: least degraded.

Table 4: Simple Vent and Pit Vent Morphometric Parameters

	Average [km]	Standard Deviation [km]	Median [km]	Mode [km]
Simple Vent Length	13.6	8.03	12	7
Pit Vent Length	13.3	9.17	9	4
Vent Depth	0.6	0.5	0.5	0.5